

NCAR Manuscript No. 492  
for review purposes only

EXPERIMENTS ON THE GENERATION OF SMALL WATER WAVES BY WIND

E. J. Plate, P. C. Chang  
Colorado State University, Fort Collins, Colorado

and

G. M. Hidy  
National Center for Atmospheric Research, Boulder, Colorado

March 1968



Abstract

The generation and growth of small water waves by a turbulent wind has been investigated in a laboratory channel. The evolution of these oscillations with fetch was traced from their inception with amplitudes in the micron range under conditions of steady air flow. The experiments revealed that the waves are generated at all air velocities in small bursts consisting of groups of waves of nearly constant frequency. After traveling for some distance downstream, these wavelets attain sufficient amplitude to become visible. For this condition a wind speed critical to raise waves is well defined. After the first wavelets appear, two new stages of growth are identified at longer fetches if the airspeed remains unchanged. In the second stage, the component associated with the dominant frequency of the wave spectrum initially grows most rapidly with fetch until it attains an upper limit of amplitude consistent with the well known equilibrium range, which appears to be universal for wind waves on any body of water. The frequency of this dominant wave in the second stage remains constant with fetch up to equilibrium, but tends to decrease with increasing wind shear on the water. In the third stage of growth, only wave components whose energy is lower than the equilibrium limit tend to increase in amplitude so that the wave spectrum is maintained at equilibrium in the high frequency range of the spectrum. We found no features of the mean air flow or its turbulence structure as characterized by the distribution of longitudinal intensity and energy spectra that could be attributed to disturbances by the first ripples. Under the shearing action of the wind, the first waves were found to grow exponentially. The growth rate agreed with the estimated from the viscous shearing mechanism of

Miles (1962a) to a fractional error of 61% or less. Slightly better agreement was obtained with the viscous theory of Drake (1967) in which Miles' model is extended to include the effect of the drift current in the water induced by the wind. But for the magnitude of the currents observed in the tunnel, this improvement is believed to be insignificant.

## 1. Introduction

It is currently accepted as a hypothesis that water surface waves are generated by a turbulent wind through a sequence of mechanisms elucidated by Phillips (1957) and Miles (1962a). According to Phillips, the initial wavelets derive from resonance between the free modes of the water surface and pressure waves set up by the turbulent eddy motion of the air flow. This class of ripples is predicted to grow linearly with time (or with fetch), until the viscous mechanism of Miles (1962a) takes over. Then the waves and the air flow become coupled; the waves give rise to a pressure distribution at the water surface which has the same frequency as the waves but is not in phase with the wave amplitude. Consequently, unless viscous dissipation exceeds the energy transferred by the induced pressure, single components of the wave spectrum grow exponentially with time or with fetch under the action of a steady wind.

A preliminary verification of the Phillips-Miles mechanism was attempted by Hidy and Plate (1966). Their data did not reveal a regime of linear growth rate on examination of the increase in spectral density of a wave component with time or with fetch. All frequency components studied initially grew approximately exponentially. However, it was found that the growth rate was not equal to that predicted by Miles (1962a), but was about twice too large. There was a certain scatter in the experimental data, but the trend towards larger growth rates than predicted analytically was quite definite.

There might have been several reasons for discrepancies between Hidy and Plate's results and the theoretical predictions in their experiments. For example, the shearing stress acting on the waves varied with fetch and a drift current in the water developed. Both of these features were not taken into account in Miles' model.

Because of the importance of learning more about the initial wavelets generated by wind, it was of interest to obtain a more precise set of measurements of the combined air and water motion. Two new experiments were designed to satisfy as closely as possible the conditions of the undisturbed mean air flow on which the Phillips-Miles model is based. In this paper results of these experiments are reported.

Experimental data indicating the nature of the turbulence over the smooth water surface and over small ripples are presented along with the results for the statistics of water surface displacement. Properties of the air turbulence were measured by well known techniques using a hot-wire anemometer. The behavior of the water waves was determined with a newly designed capacitance gauge capable of detecting undulations of the water surface to less than ten microns in amplitude.

The development of waves is discussed for conditions of measured air flow over water both for the earliest stages of growth, when the water is virtually glassy smooth, and for conditions where waves and ripples are seen easily.

The observed development of the first waves by wind action failed to agree with predictions based on the Phillips (1957) mechanism. Hence, some supplementary experiments on the role of turbulence on wave generation were performed. In addition, the influence of the drift current in the water are introduced as possible contributions to the generation and growth of wind waves. In the latter case, Drake's (1967) modification of Miles' theory accounting for the presence of a water current is applied to the observations.

## 2. Experimental Equipment and Procedures

The experiments were performed in a wind-water tunnel which has been described in detail by Plate (1965). The experimental arrangement is shown in Fig. 1. Air flows from the tunnel inlet over a smooth flat plate of 3.7 m length onto a body of initially standing water, 11.4 cm deep and 13.7 m long. The fetch  $x$  is measured positive downstream from the junction between the plate and the water. The flat plate consists of smoothly sanded aluminum. Screens and a honey comb section placed at the tunnel inlet assure an aerodynamically smooth flow developing over the bottom corresponding to flow in a developing turbulent boundary layer.

Measurements taken in this study include records of the water surface displacement, profiles of mean air velocity, turbulent fluctuations of the longitudinal component of the air flow, apparent critical wind speeds, and velocities of the drift current at the water surface. To measure the water surface displacement, a capacitance gauge was used which consisted of a 32-gauge, nyclad insulated, magnet wire combined with a bridge circuit developed in the Engineering Research Laboratories, Colorado State University. This capacitance device had a sensitivity which permitted the measurement of water surface undulations with amplitudes of less than ten microns. For such low amplitudes, even a wire as thin as the one employed here is not free of capillary adhesion effects. Consequently the data should be accepted with reservation at lowest wind speeds until verified by other investigations. At the high wind speeds, however, the wave heights were significantly larger than ripples found in lower wind speeds even at the shortest fetches, so that the results can be used with confidence.

The capacitance probe was practically free of drift in the bridge circuitry. A tendency for drift was observed only at the very highest sensitivities, and over much longer times than any sampling time used.

The data of wave amplitude were recorded on a Brush Mark III strip chart recorder (with a frequency response curve flat to 30 Hz) and were digitized manually for computer analysis. Calculations of the statistical properties of the wave records included the standard deviation  $\sigma$ , the autocorrelation function  $R(\tau)$ , and the energy spectral density  $\phi(n)$ . For such computations, techniques were used which have been described previously by Hidy and Plate (1966).

Mean velocity measurements in air were made by continuously recording on an x-y recorder the dynamic pressure of a pitot-static tube versus signal proportional to the distance from the undisturbed water surface as the probe moved vertically through the air stream. Turbulent fluctuations were measured with a hot wire anemometer made by the Hubbard Company, working on a constant temperature principle. The probe containing the (hot) wire was held stationary at a given position for five minutes while the root mean square (rms) value of the signal was read, the turbulence signal was recorded on an FM tape recorder. The rms meter used measured 99% of the fluctuating signal (above) 2 Hz. The spectra of these records were determined with a Bruel and Kjaer analog spectrum analyzer, type 2109, with proportional one-third octave filters. The low frequency range of the spectrum was investigated more closely with a spectrum analyzer made by Technical Products (type TP 627) which has constant band width filters of 2 Hz with a continuously variable center frequency.

It was found that a critical wind speed could be defined at a given fetch as the speed of the air at a fixed reference location at which the vibrations of the water surface became visible. During such a test, the water surface was observed by watching the reflections of the capacitance wire it, as indicated in Fig. 2. At wind speeds below critical the reflection was a straight line which, with increasing wind speed, first oscillated irregularly in time with ever increasing amplitude and then disrupted. The critical wind speed was defined rather arbitrarily as the speed where the reflection was still sinusoidal but on the verge of transition to the disrupted stage as shown in Fig. 2b.

Velocities of the drift current at the water surface were measured by observing the motion of disks of 0.6 cm in diameter cut from thin wax paper, and timing the passage of the paper particles between distance markers. The distance markers consisted of strips of adhesive tape glued to both transparent walls of the wind-water tunnel across which the passage was sighted. At the time of passage, a switch was thrown which would apply a voltage to a voltage-time recorder. At the passage of the next strip, the switch was thrown again, and a downward step was obtained. In this manner, a single particle could be timed at all marks along the channel. Twenty particles were traced and averaged for the determination of each case of water surface speed.

### 3. Results

#### 3.1 Air Motion over Very Small Waves

To test the applicability of the theoretical calculations to wave generation in the tunnel, experimental conditions were restricted primarily to cases when the shearing stress at the water surface was constant with fetch and time and the disturbances on the water surface were as small as possible yet still observable. For completeness, however, and for comparison with previous work, a few measurements of air flow and water surface agitation are cited in a range where the surface stress increases downstream with the influence of the growing waves. The reason for confining attention mainly to conditions where the waves are very small and the surface stress is uninfluenced by the induced surface roughness, is that virtually all analytical models assume no coupling or weak coupling between the air and water motion. Let us begin by presenting typical aerodynamic data to show that such conditions existed over the regimes of principal interest in so far as we were able to determine with the experimental equipment.



Mean velocity profiles. Two different regimes of air flow were examined in this study, one at low wind speed in the "critical" regime of  $u_{\infty} \approx 3$  meters-sec<sup>-1</sup>, and one at higher wind speed of  $u_{\infty} \approx 11$  meters-sec<sup>-1</sup>. Here  $u_{\infty}$  refers to the speed of the air stream outside the boundary layer, whose thickness  $\delta$  is defined as the height at which the mean wind speed  $\bar{u}$  is equal to  $0.99 u_{\infty}$ . All of the measured wind profiles are well correlated by a logarithmic form:

$$\frac{\bar{u}(y)}{u_*} = \frac{1}{K} \ln y/z_0 \quad (1)$$

where  $u_*$  is the square root of the ratio of the stress at the water surface to the air density  $\rho_a$ . Karman's constant,  $K$ , is taken as 0.40, and  $z_0$  denotes the roughness length. Typical parameters for the mean air flow are listed in Table 1.

In the low speed cases, waves could be identified visually only downstream of the critical fetch, while at the higher wind speeds, waves appeared immediately after the edge of the aluminum plate. At all wind speeds, the distributions of average longitudinal velocity were found to be linear with logarithm of height in the lower portion of flow. At distances far downstream in the high speed flow, departures from the logarithmic profile were observed, but this regime will not concern us here. In cases where the wind profiles were logarithmic,  $u_*$  was estimated from the slope of the lower portion of the profile. Because of the rapid growth of waves at the higher wind speeds,  $u_*$  remained constant under these conditions only for a fetch  $x \leq 50$  cm. These results previously have been discussed for slightly different conditions of air speed by Plate and Hidy (1967).

Eq. (1) is often written in the form of the law of the wall:

$$\frac{\bar{u}(y)}{u_*} = \frac{1}{0.40} \ln \frac{u_* y}{\nu_a} + \text{const.} \quad (2)$$

where  $\nu_a$  is the kinematic viscosity of the air, and the constant is related to the roughness length,  $z_0$ . Typical mean velocity profiles in the air are shown in this form in Fig. 3. The constant in Eq. (2) found for flow over the aluminum plate is 5.6, which is

Table 1

## Typical Characteristics of the Mean Flow of Air

$x$ (cm)	$u_{\infty}$ (m-sec <sup>-1</sup> )	$u_*$ (cm-sec <sup>-1</sup> )	$\delta$ (cm)	$z_0$ (cm)	Remarks
488	3.66	15.8	7.62	$9.6 \times 10^{-4}$	critical fetch, without grid
488	3.20	13.4	5.72	$11.2 \times 10^{-4}$	critical fetch, with grid
-35.3	10.6	45	4.8	$3.3 \times 10^{-4}$	over plate
244	11.1	62.4	6.8	$8.02 \times 10^{-3}$	over initial ripples ( $\sigma \approx 0.3$ cm)
850	12.8	82.5	15.0	$3.82 \times 10^{-2}$	over fully developed waves ( $\sigma \approx 0.9$ cm)

somewhat larger than the value of 4.9 quoted by Clauser (1954) but it has been observed by many workers that this constant can vary over a range between 4.3 and 6. The two profiles shown for larger fetches agree with Eq. (2) except for the numerical constant, which is found to be negative. This is typical for flow over fully rough boundaries. Corresponding values of  $z_0$  are given in Table 1.

For wind profiles taken at low speed over water, the constant in Eq. (2) was found to be equal to 6.1. The agreement with the results for flow over solid boundaries could be improved by considering the air flow relative to the velocity of the drift current at the surface,  $u_s$ . By substituting  $\bar{u} - u_s$  for  $\bar{u}$  in Eq. (2), one obtains close agreement with the value of using  $u_s/u_* = 0.57$  obtained from observations of surface drift at this wind speed.

The two distributions taken at low speeds in Fig. 3 correspond to the critical condition where waves appeared by the optical criterion at a fetch  $x = 488$  cm. One set of data was obtained with a flow developing with inlet conditions normally set up in the tunnel. The second set of data was taken under inlet conditions modified by placing at the upstream edge of the aluminum plate a heavy grid of slats 2.54 cm wide nailed crosswise at distances of 5.08 cm. The two conditions of low wind speed correspond to different boundary layer thicknesses, and different velocities in the free stream as well as different shearing velocities (Table 1). The reason for modifying the inlet conditions was to change the characteristics of the air turbulence. This aspect of the study will be discussed later.

Turbulence properties. The properties of the turbulent fluctuations in the longitudinal component of the air velocity were estimated from the hot wire anemometer measurements. The variance of the turbulent fluctuations,  $\overline{u'^2}$ , was measured as a function of height from the mean water level for the high ambient

air speed over several different fetches. These results are shown in non-dimensional form in Fig. 4a. The quantity  $(\overline{u'^2})^{1/2}$  has been normalized by  $u_*$  and plotted with  $y/\delta$ . The data taken at high wind speed over the plate is in satisfactory agreement with Klebanoff's results except in the outer portion of the boundary layer where the higher free stream turbulence caused deviations. The intensity profiles over the waves are similar in shape to that of Klebanoff (1954), but the dimensionless intensities are somewhat larger for a given thickness  $\delta$  because the shearing flow evidently is not in equilibrium with the roughening surface. Our results, of course, could be brought into better agreement with Klebanoff's by an adjustment in the value of the boundary layer thickness.

In the observations of air turbulence taken at critical fetch, the boundary layer thickness is not a meaningful scaling parameter because the change in the free stream turbulence significantly distorts the outer part of the boundary layer, leading to a thickness which is much smaller than that for the very similar flow conditions without the grid turbulence superimposed. Since the two cases differ in shear velocity only by 15%, the profiles of intensity are approximately similar in the lower boundary layer if plotted in dimensionless form based on the similarity parameters of the mean flow as given by Eq. (2). In Fig. 4b curves for  $(\overline{u'^2})^{1/2}/u_*$  vs  $y u_*/\nu_a$  are drawn, showing striking agreement between the two cases near the boundary. In the outer part of the boundary layer the grid turbulence, of course, influences the intensity profile strongly.

Results in Fig. 4b for the turbulent intensity display an apparent systematic variation with Reynolds number, as suggested by comparison between Laufer's (1954) data for pipe flow, and Klebanoff's (1954) results in a wind tunnel.

From analysis of magnetic tape recordings of the signal from the hot wire anemometer, energy spectra for the longitudinal

component of air flow were determined. Some typical examples plotted in frequency coordinates are shown in Fig. 5. These spectra represent data taken at critical conditions for the visible onset of waves at a fetch of  $x = 350$  cm, for  $u_{*} = 17$  cm-sec<sup>-1</sup> ( $u_{*} = 4.0$  m-sec<sup>-1</sup>). They display a distribution of turbulent energy with wave number that is characteristic of known turbulent flows (e.g., Hinze, 1959).

The modification of the energy distribution by changing inlet conditions is readily seen in the examples of Fig. 5. At elevations close to the water surface, say  $y = 1.27$  cm, the spectra were influenced by the presence of the grid mainly in the low wave numbers (low frequencies). The relatively high level of turbulence in the outer portions of the boundary layer induced by the grid tended to be associated with the large eddies, while at higher frequencies the energy distribution is nearly the same with or without grid. Consistent with the well known idea of persistence of large eddies, the energy density associated with low frequency regime does not change much with height. The variation in energy distribution with height is mainly the result of decreases with elevation in energy density in the smaller scale motion. It is interesting that in the case with the inlet grid, the higher level of turbulence in the free stream was accompanied by much smaller decrease with height in energy over all frequencies in contrast to other cases.

Apparent rates of energy dissipation were calculated based on the assumption of isotropy in the small scales of turbulent motion. For this assumption, the dissipation rate  $\epsilon$  per unit mass becomes (Hinze, 1959):

$$\epsilon = 15 \nu_a \overline{\left( \frac{\partial u'}{\partial t} \right)^2} \frac{1}{u'^2} \quad (3)$$

Instead of evaluating  $(\partial u'/\partial t)$  directly, we have used the one-dimensional energy spectrum, and have evaluated  $(\partial u'/\partial t)^2$  from it through the relation

$$\overline{\left( \frac{\partial u'}{\partial t} \right)^2} = (2\pi)^2 \overline{u'^2} \int_0^\infty n^2 F(n) dn \quad (4)$$

Here  $n$  is the frequency in Hz, and  $F(n)$  in sec. is the spectral density of turbulent energy in the frequency domain.

The spectral technique for calculating dissipation rates has also been employed by Pond, et al. (1963) for turbulent winds over ocean waves. Since it is of interest to compare our data with theirs, the dissipation rates have to be defined on the same basis. However, the validity of the assumption of local isotropy in turbulent shearing layers is open to question. Klebanoff (1954), for example, has found that direct evaluation of dissipation rates in the boundary layer along a flat plate near the wall yielded about twice the rates estimated on the basis of the assumption of isotropy. Typical values of dissipation rates calculated from Eqs. (3) and (4) are listed in Table 2 along with values of the microscale  $\lambda_g$  calculated from:

$$\lambda_g^{-2} = \left( \frac{2\pi}{u} \right)^2 \int_0^{\infty} n^2 F(n) dn. \quad (5)$$

Distributions of  $\mathcal{E}$  as function of height and fetch for the case of high wind speed are shown in Fig. 6. Here data of Hess (1968) are also given for comparison. Both sets of data are seen to be consistent. A strong increase in the apparent dissipation rate with fetch is observed in these results. The dissipation rate increases faster than production. If as a first approximation, production is set equal to dissipation rate then one should obtain in the constant stress layer with  $\overline{u'v'} \approx u_*^2$  that  $\mathcal{E}ky/u_*^3 = 1$ , where  $v'$  is the fluctuation of the vertical component of velocity. If this number is larger than 1, then dissipation exceeds production. If it is smaller than 1, production exceeds dissipation and the turbulent intensity increases with distance. Calculated values of  $\mathcal{E}ky/u_*^3$  are listed in Table 2. Although this increase in dissipation rate is more rapid than the increase in production, the absolute magnitude of production is found to be larger with fetch, and only at the largest fetches is a balance found near the surface.

Table 2

## Typical Turbulence Characteristics of the Air Motion

x (cm)	y (cm)	$u_*$ (cm-sec <sup>-1</sup> )	$\overline{(u'^2)}^{\frac{1}{2}}$ (cm-sec <sup>-1</sup> )	$\epsilon \times 10^{-4}$ (cm <sup>2</sup> -sec <sup>-3</sup> )	$\lambda_g$ (cm)	$\frac{\epsilon \eta y}{u_*^3}$
350 (without grid)	1.27	17	11	1.20	0.43	1.24
	2.54		7.9	0.75	0.54	1.55
	7.62		2.6	0.16	0.66	0.99
	12.7		1.0	0.07	0.66	0.725
350 (with grid)	1.27	15.8	7.0	1.42	0.37	1.82
	2.54		4.0	0.42	0.51	1.08
	7.62		1.5	0.20	0.58	1.55
-35.3 ( $\delta=4.8$ cm)	0.51	45	114	17.0	0.48	0.38
	1.14		75	4.6	0.58	0.23
	2.42		56	1.8	0.71	0.19
	3.69		33	.76	0.64	0.12
	6.22		10.2	.033	0.94	0.09
244 ( $\sigma \approx 0.3$ cm)	1.27	62.4	127	16.8	0.51	0.36
	1.91		118	14.4	0.52	0.45
	2.54		111	11.1	0.55	0.46
	3.82		92	5.5	0.66	0.34
	5.08		75	3.0	0.73	0.24
850 ( $\sigma \approx 0.9$ cm)	4.42	82.4	161	29.8	0.48	0.98
	5.69		150	25.0	0.50	1.01
	6.96		134	16.5	0.55	0.81
	8.86		120	11.0	0.60	0.69
	14.0		69	2.7	0.70	0.29

In contrast to the case of higher wind speed, one finds that the dissipation rates are markedly higher at the low wind velocities (critical fetch cases). The fact that  $\epsilon$  exceeds production of  $u_*^3/\nu y$  near the surface is in contrast to the finding over a smooth plate such as at  $x = -35\text{cm}$  (Table 2). Even though measurement errors at these low velocities are particularly large, it is not likely that they cause almost an order of magnitude error, so that the difference between the observed data and smooth flat plate behavior is attributable to the presence of the water surface.

The turbulent energy spectra calculated for flow over the waves could be represented non-dimensionally over most of the high wave number ranges by a similarity profile. The scaling parameters were those required by Kolmogoroff's inertial subrange. The dimensionless spectrum is given by

$$\psi(k/k_s) = B F(n), \quad (6)$$

where

$$B = \frac{\bar{u} \overline{u'^2}}{2\pi} (\epsilon \nu_a^{-5})^{-1/4} \quad (7)$$

and  $k_s = (\epsilon \nu_a^{-3})^{1/4}$ . Spectra recalculated in this framework for several fetches, using  $\epsilon$  from Eq. (3) are shown in Fig. 7.

All spectra shown have a well defined viscous dissipation range at the high wave numbers. In this range, the spectra fall on the same curve, which agrees with the universal form found, for example, in thicker turbulent layers by Sandborn and Marshall (1965). Adjacent to the low wave number extreme of the dissipation range, there may exist an inertial subrange. Pond, et al. (1963) found that for spectra over ocean waves the  $k^{-5/3}$  decrease holds over many decades of wave numbers. Their average curve has been plotted with the experimental spectra of Fig. 7. The case of relatively large intensity of turbulence in the free stream; i.e., the case critical velocity at  $x = 3.50\text{ m}$  with grid upstream of the plate produced the inertial subrange which resembles most closely that found by Pond, et al. This is typically observed when laboratory data and that taken on geophysical scales are compared.



For the conditions of low free stream velocity, or for conditions near the outer zone of the air flow responding to changing surface roughness, the Kolmogoroff constant  $K$  as defined by

$$\psi(k/k_s) = K (k/k_s)^{-5/3} \quad (8)$$

deviates from the value of 0.46 reported by Pond, et al. The value of 0.46 probably corresponds to a turbulent medium which is in local equilibrium as specified by the dissipation rate  $\epsilon$  equalling the production rate.

### 3.2 Wind Induced Water Motion

The measurements of the turbulent shearing flow in air over the water characterize the conditions for energy transfer to the water. Under the influence of the air motion, waves are raised, and a drift current develops.

The wind waves. As the steady wind is gradually increased in speed from zero, the water surface at any given point undergoes gradual changes from glassy smooth to being agitated with fully developed waves. This is illustrated by the sequence of photographs shown in Fig. 8. The first waves, identified near critical conditions in Fig. 8, are smooth undulations, two-dimensional in appearance, which are oriented with crests nearly perpendicular to the direction of flow (Fig. 8a, and 8b). As the wind speed increases, the water surface becomes somewhat more ruffled (Fig. 8c, 8e, and 8f). Short crested ripples are superimposed over the first undulations (Fig. 8c, 8e) and the wave pattern looks more rhombic in appearance. With further increase in velocity the rhombic pattern evident in Fig. 8c, 8e, and 8f reorders itself into a more two-dimensional wave pattern where the waves are slightly skewed with longer and smoother backs than fronts (Fig 8d, 8g, and 8h).

The ripples which were originally distributed rather uniformly over the surface become concentrated on the wave fronts and align to form more or less uninterrupted ridges in front of the wave crest. They have a maximum amplitude near the crest of the wave, on which they are superimposed, and diminish in size towards the valley of the large wave where they disappear altogether. The ripples have a wave length which lies between 0.5 and 1 cm, and they appear to stay with the larger wave on whose front they ride. The general appearance of the water surface is then as shown in Figs. 6f and 6h. In Fig. 6f, the ordering process of the ripples has just begun, and in Fig. 6h it is essentially completed. The pattern is thus seen to be similar to the development described qualitatively by Phillips (1966).

If the wind speed  $u_{\infty}$  is increased beyond  $10 \text{ m-sec}^{-1}$  the early evolution of ripples pictured in Fig. 6a, 6b, and 6h is not so easily observed. Instead, it is compressed into a zone of fetch very near the inlet plate. This can be seen in Fig. 9. At longer fetches at high wind speed, the capillary ripples are observed to emerge both on the windward and leeward sides of the two-dimensional, dominant waves, as observed earlier by Hidy and Plate (1966).

The records of water surface displacement taken at one point under conditions similar to those for the photographs in Fig. 8 are shown in Fig. 10. They were taken at  $x = 3.5 \text{ m}$  for different wind speeds around the critical value. They give further information about the nature of the onset of visible waves on the water surface. Two striking features are revealed in the traces of Fig. 10. First, the recordings show quite clearly that microscopic undulations exist at velocities well below the critical value even though they are not optically significant. Even at the lowest wind velocities occasional bursts of tiny wavelets were observed whose amplitudes exceeded the sensitivity threshold of the capacitance gauge. It can therefore be concluded that waves exist at practically all wind velocities. However, in order to become identifiable as waves they must have grown under the influence of the wind; i.e., they must have

traveled downstream for sometime. At critical conditions, these first undulations appear visually to be on the verge of breaking up into the rhombic pattern.

Secondly, it is observed that the process of wave growth takes place in the following manner. At the lowest wind speeds, the apparently calm surface is occasionally interrupted by the passage of a small group of waves which are just of sufficient height to penetrate the sensitivity threshold of the capacitance gauge. With increase in wind speed, the wave groups accumulate more waves, but grow only very little in amplitude until the groups join and form irregular interference patterns near their joints. Further increase in wind velocity leads to a growth in amplitude of particular waves which is again followed by adjustment in height of the adjacent waves. This process appears to repeat itself with increasing wind speeds, so that it is always possible to distinguish well separated groups of waves, displaced with respect to each other by random phase shifts, but well defined and quite regular in themselves.

In addition to the records in Fig. 10, a series of wave gauge traces were taken upstream and downstream of the critical fetch at constant wind speed. A typical set of spectra  $\phi(n)$ , where is the density of the potential energy of the Fourier component associated with frequency  $n$ , calculated from such data are drawn in Fig. 11. At fetches smaller than critical, the wave spectra are diffuse in the low frequency range, falling off at high frequencies. The broadness of the spectra in this range may be an indication of the noise level and averaging or sampling error inherent in the digital analysis rather than of the presence of many Fourier components of nearly equal energy in the agitated surface. Just beyond the critical fetch, the spectra begin to sharpen up as energy is transferred at a maximum rate to a narrow band of waves whose frequency is centered around 8.5 Hz. With increasing fetch, the spectrum remains nearly constant in shape and has its maximum at 8.5 Hz until the peak reaches a curve which denotes an

equilibrium limit. The equilibrium range is a curve denoted by (Phillips, 1966)

$$\phi(n) = \beta g^2 n^{-5} \quad (9)$$

where  $g$  is the acceleration of gravity,  $n$  is given in Hz, and  $\beta$  is the constant of proportionality, approximately equal to  $7.5 \times 10^{-6}$ . This equilibrium range has been found to exist for waves varying from those observed on laboratory scales to ocean waves. Growth of a frequency component far beyond the equilibrium limit denoted by Eq. (9) does not appear possible on theoretical grounds. Instead, a continued increase in energy of a wave train at this stage tends to be associated with a shift of the spectral peak to lower and lower frequencies (See also Appendix).

Despite theoretical arguments for not exceeding the equilibrium limit of the wave spectrum, observations such as Sutherland's (1967) indicate that Fourier components may overshoot this limit, but will return to it rather quickly (See also Fig. 13).

The shape of the developing spectra below the equilibrium or saturation level, especially in the high frequency range, is of interest. The decrease with  $n$  of these curves follows a power law somewhat steeper than  $n^{-5}$ , but as the equilibrium is approached by the peak frequency, the slope of the envelope to all spectral curves tends to the  $n^{-5}$  decrease. We believe that two different processes may be involved in shaping the wave spectra. The equilibrium range, denoted by Eq. (9), is a physical limit to the growth of the dominant wave probably related to the maximum steepness which a wave can have without necessarily implying wave breaking as postulated earlier by Phillips (1958) (See Appendix). On the other hand, the drop-off of the spectrum at high frequency at a rate proportional to  $n^{-5}$  might be a spurious result introduced by the Blackman and Tukey (1958) method for calculating spectra. Since pre-whitening is usually not employed and was not used here, a small amount of energy may drain from the dominant peak into the side lobes of the spectral windows.

While for peak spectral densities below equilibrium the frequency remains constant at constant shear velocities, it is observed that an increase in wind velocity has a tendency to shift the peak of the unsaturated wave spectrum to lower frequencies. In a set of experiments ranging from  $u_* = 17$  cm/sec to  $u_* = 35$  cm/sec the peak was seen to move from 7 to 11 Hz. The results are tabulated in Table 3. The experiments also lead to a decrease in fetch length at which critical conditions for wave appearance were observed until beyond  $u_\infty \sim 6$  m-sec<sup>-1</sup> waves developed off the trailing edges of the inlet plate (Fig. 9).

An illustration of the spectra found under conditions of higher wind speeds is shown in Fig. 12. These data correspond to the evaluation of the agitated surface at  $u_\infty \sim 10$  m-sec<sup>-1</sup>. Close to the plate at  $x \lesssim 5$  cm, the spectra display a peak at  $n = 16$  Hz which is attributed to the tunnel vibrations. The natural vibrations of the tunnel were examined and found to be nearly sinusoidal with a frequency of about 18 Hz, governed by the rotational speed of the fan. The 16 Hz peak is quite pronounced at  $x = 1$  cm. By  $x = 5$  cm, this component has become secondary in importance to a wind induced component at a frequency of about 11 Hz. At fetches up to 50 cm, the 11 Hz component is predominant in the spectra. In this case, therefore, it appears that this component represents the wave of maximum growth over a fetch of from 0 to 50 cm. For this fetch a constant shearing stress of  $u_* = 35$  cm-sec<sup>-1</sup> was determined as previously reported by Plate and Hidy (1967). At a fetch of about 40 cm, the 11 Hz component reaches the equilibrium curve, and from then on the frequency associated with the dominant peak decreases with increase in fetch, as has been observed in the case of flow at low velocities. In contrast to the case shown for low wind speed in Fig. 10, the high frequency range of the spectra realize an  $n^{-4}$  to  $n^{-5}$  decrease even before attaining equilibrium.

Table 3

Increase in Frequency of Spectral Peak with Wind Speed  
in the Second Stage of Growth

$u_*$ (cm-sec <sup>-1</sup> )	Frequency of spectral peak $n_{\max}$ (Hz)	Predicted frequency of spectral peak based on Miles' theory with wave number corrected for drift current (Hz)
15.8	7.0	9.2
16.2	7.0	-
17.0	7.5	9.2
19.0	8.5	9.3
19.8	9.0	-
35.0	11.0	12.8

Series of spectra taken at increasing fetches such as those shown in Figs. 11 and 12 enable the tracing of the growth of a particular Fourier component. Two results of this kind are shown in Fig. 13. These curves indicate that the 11 Hz component of the high wind spectra follows an exponential growth law up to about 40cm fetch when equilibrium is attained. The growth rates for the spectra taken for conditions of low wind speed generally were not nearly as well defined. The case for  $u_* = 19 \text{ cm-sec}^{-1}$  in Fig. 13 displays a region upstream of the critical fetch,  $x = 60 \text{ cm}$ , where the growth rate is small. However, from about  $x = 100 \text{ cm}$  to conditions where equilibrium is attained for the 8.5 Hz component at  $x \approx 300 \text{ cm}$ , the spectral density increase is best fit by a straight line of slope  $6.5 \text{ meters}^{-1}$ , suggesting an exponential growth up to the equilibrium limit. An illustration of overshoot of  $\phi(n_{\text{max}})$  before attaining equilibrium regime is indicated in the data for  $u_* = 19 \text{ cm-sec}^{-1}$ .

The drift velocity at the water surface. The velocity  $u_s$  of the water surface was measured by means of the technique described earlier in Sec. 2. Results are shown in Fig. 14 for two different friction velocities based on the air motion. It is observed that over short fetches the drift velocity increases roughly according to a power law, while at fetches exceeding about 1 m, the ratio of drift velocity to the free stream velocity,  $u_s/u_\infty$ , attains a constant ratio of 0.026. If a cross-sectional average wind speed is defined as  $0.8 u_\infty$ , these results agree with data obtained by Keulegan (1951) for large Reynolds numbers based on fetch.

#### 4. Discussion

When air flows from a smooth solid surface onto water the turbulent boundary layer evolves in essentially the same manner as it would have over an inflexible boundary. As long as the wave amplitudes do not exceed  $\sigma \approx 0.15 \text{ cm}$ , the structure of turbulence

remains characteristic of shearing layers over smooth boundaries (See also, Plate and Hidy, 1967). For waves of larger amplitude, the wind profile responds in its lower parts to the increasing roughness in a manner predictable from calculations based on a solid surface. For our present data, examination of the mean flow, turbulent intensities and energy spectra of the longitudinal component, and apparent turbulent energy dissipation rates suggest no marked anomalies attributable to wave action on the air even over ripples whose standard deviation exceeds 0.1 cm., except possibly for the dissipation rates. Since the wind field is at most weakly affected by the water waves, and since a region of constant shear with fetch can be realized, it should be possible to compare the data taken in the tunnel with predictions based on theoretical models such as Miles' (1962a). In the following sections we shall discuss the experimental results principally in the light of such theoretical concepts.

#### 4.1 Stages of Development of the Small Waves

The experimental observations showed that there are three distinguishable regimes in the evolution of surface waves. The first is a condition wherein essentially two dimensional microscopic disturbances form on a nearly glassy surface. These tiny oscillations have a regular shape with crests oriented nearly normal to the wind direction, and with a well defined frequency (Fig. 8a, 8c, and Fig. 10), which depends on the magnitude of the shearing stress exerted on the water surface by the wind.

If the wave crests of the nearly microscopic disturbances were not oriented perpendicular to the wind, a marked change in dominant frequency in the records of Fig. 10 would appear after waves became visible. In the latter case, the visible dominant waves were quite distinctively oriented with crests normal to the wind direction as shown in Fig. 8a and 8b. The regularity in appearance of the



first waves at frequencies lower than 13 Hz suggests that the resonance mechanism of Phillips (1957) may be relatively unimportant in setting up the initial disturbances. This conclusion is strengthened by the observation that in none of the data could a linear growth rate be unambiguously identified as predicted by Phillips' model. Other results of supplemental experiments discussed below also bear on this conclusion.

In the second regime of development, the wave pattern evolves spontaneously into a cross-hatched pattern of three dimensional configuration (Figs. 8c, and 8e). This change in pattern, however, cannot be detected directly in wave traces taken at only one point. In such measurements, two dimensional disturbances have the same appearance, and the same dominant frequency as the rippled, more three dimensional configuration.

The appearance initially of two growth stages characterized by two dimensional oscillations supplanted by three dimensional wavelets also was recognized by Cohen and Hanratty (1965) for wind ripples on thin layers of liquid.

The third regime is associated visually with a return to a pattern of more or less two dimensional gravity waves on which are superimposed small capillary ripples (Fig. 8d, 8g, and 8h). This regime is characterized by amplitude spectra which coincide with a "universal" equilibrium range in the high frequencies (Fig. 11 and 12). The third regime of wave development appears to be the one best studied in previous investigations, and it seems to be the one of principal significance in relation to ocean waves, or lake waves.

Present theoretical knowledge seems to be able to explain qualitatively the broad aspects of wind action on a water surface, particularly in the first regimes of growth after the onset of microscopic disturbances. However, the theory for describing the growth of waves once the equilibrium range is attained is not entirely satisfactory at this time. Furthermore, the origins of the first two-dimensional ripples on a microscopic scale cannot be considered explained at present. In an attempt to obtain

further insight into the nature of the onset of the first disturbances in the water, two supplemental experiments were performed.

#### 4.2 Experiments on the Role of Pressure Fluctuations in Wave Initiation

Two tests were performed on the effect of changes in the turbulence structure in the air on the process of wave generation. At the same time the ambient wind velocity with the grid was decreased to  $3.2 \text{ m-sec}^{-1}$  as compared with  $u_{\infty} = 3.7 \text{ m-sec}^{-1}$  for the same case without the grid, maintaining a critical fetch at 4.88 m where waves first became visible in the sense of the criterion described in Sec. 2. In the first, the turbulence level of the air was significantly changed (Fig. 4b and Table 2) by inserting the grid into the air flow a short distance up-wind of the inlet plate while maintaining a constant critical fetch. The mean velocity distributions and turbulence intensities from these tests were compared with equivalent results obtained for the same critical fetch but without grid. The experimental data on the mean velocity distributions shown in Fig. 3 do not indicate any differences in shape of the velocity profile or any significant changes in the nature of the shearing flow. Rather the profiles correspond in both cases to that for flow over a smooth solid boundary. The observed change in shearing velocity  $u_{*}$ , or shear stress  $\tau_0$  is significant, however. The shear stress for the case without grid is approximately 40% larger than that for the case with grid. Yet the turbulent intensity profiles shown in Fig. 4b coincide in the lower portions for both cases if nondimensionalized by means of scaling based on the shear velocity. Hence, within the shearing layer, the turbulent intensity at a given elevation above the water surface is actually lower for the case with grid, but outside the boundary layer, the intensity was larger. A set of spectra of the turbulent energy for the same elevation above the water surface, shown in Fig. 5, indicates that the difference between the two cases is found in the low frequency end of the spectra. The

high frequency ends of the spectra are identical. At the low frequency end of the spectrum where the energy associated with water waves should be found, the spectral energy of the case with grid is much lower.

The results of this experiment suggest that for a given wind speed, a higher turbulent intensity in the ambient air outside the boundary layer leads to an earlier triggering of the disturbances of the water surface. An analogy with transition to turbulence in a boundary layer, which also can be triggered by increasing the level of the turbulent intensity in the free stream, suggests itself. However, in our experiments, the air flow is turbulent already even at the shortest fetches. Tollmien-Schlichting waves in the air must therefore be ruled out as initiators of the first water surface waves. Thus, if the initial waves are a result of a transition from laminar to turbulent motion, it can only be a transition in the water. In the first meter or so the flow in the water appears to be laminar in nature, but further downstream a transition to turbulent flow takes place. This was ascertained from observations of hydrogen bubble traces released in the water near the surface at conditions of critical fetch of 3.5 meters. At low air velocities, the bubble pattern passed through a stage where small low frequency oscillations apparently associated with secondary circulation are the only observed disturbances of the water current near the surface. With increasing wind speed conditions are attained in which an occasional large eddy sheds from the thin layer of accelerated fluid near the surface into the interior of the water. At still higher wind speeds when the first waves become visible at the surface, the flow near the surface exhibits the eddying characteristics of fully turbulent motion. Nevertheless, the conclusion that waves on the water surface result in response to Tollmien-Schlichting waves in the water is probably not justified, since the disturbances for which the water boundary layer becomes unstable should travel with a progression speed which is lower than the surface velocity, so that the critical layer at which the current velocity equals

the phase speed of waves would be found in the water. This is contrary to observation which shows that all waves travel with phase speeds exceeding the water surface velocity.

The ambiguities in interpretation of these results might be resolved by postulating an initiation mechanism which produces comparatively well ordered large scale and low frequency pressure oscillations associated with the air turbulence in the outer portion of the boundary layer. Such oscillations might develop a resonance with free modes of the water surface, equivalent to the mechanism of resonant interactions predicted by Phillips (1957). In general the pressure pattern of a turbulent medium has been found to be related to the  $(u^1)^2$  pattern. Willmarth and Wooldridge (1962) have shown a large degree of correlation between pressure fluctuations and fluctuations in the longitudinal component of the air velocity. They found that the propagation velocity of the pressure disturbances in a shearing flow was equal to that of the velocity fluctuations. Furthermore, the space-time correlation functions between pressure and velocity were quite similar in shape and scale to those of the component of turbulent velocity,  $u^1$ . These conclusions have been placed on a more theoretical foundation recently by Bradshaw (1967). Based on arguments that the large eddies of the turbulence are axisymmetric, Bradshaw deduced that the pressure spectrum and the  $(u^1)^2$  spectrum in the outer portion of the boundary layer should be identical at low frequencies. Consequently, a study of the low frequency end of the  $u^1$  intensity spectrum should yield information on the pressure fluctuation at corresponding frequencies. Since most of the energy of the spectrum is associated with low frequencies, the average progression velocity of the spectrum is governed by the average progression velocity of the low frequency components. Thus measurements of the average progression velocity of the turbulence intensity pattern can be interpreted in terms of the mean progression velocity of the low frequency fluctuation in pressure.

A second experiment was therefore designed to check indirectly for the possibility of finding low frequency pressure waves moving at the phase velocity of observed modes of the surface waves by measuring the progression velocity of the  $u^1$  intensity pattern from space time correlations such as the example shown in Fig. 15. To obtain these curves, a hot wire probe was embedded into the aluminum plate 12.7 cm upstream of the beginning of the water surface and was elevated to 2.5 cm in the approaching air stream and thus was well into the outer portion of the boundary layer. At the same elevation, but downward from this fixed probe, a movable probe was located at various distances such that the distance (x) between the two probes was varied from 2 to 30 cm. At a given probe spacing, the two hot wire signals were recorded simultaneously on the FM tape recorder. The space-time correlations were calculated by analog techniques using the relation:

$$R_o(\tau, x) = \frac{1}{u'^2 T} \int_0^T u'(t, x_o) u'(t+\tau, x_o+x) dt, \quad (10)$$

where x is the location of the fixed probe,  $\tau$  is the delay time of one signal with regard to the other, and T is the averaging (sampling) time.

From the space-time correlations a curve of the progression velocity  $u_p$  is found by plotting the delay time  $\tau_p$  corresponding to the peak correlation vs. distance x, and determining  $u_p$  locally by the definition  $u_p = dx/d\tau_p$ . The progression velocity was found to be constant and about equal to  $0.8 u_\infty$  ( $8.5 \text{ m-sec}^{-1}$ ), which is well above the phase velocity of any observed waves.

From the data in Fig. 15 we note that the turbulent flow pattern is quite persistent. At a distance x of 30 cm, the maximum correlation coefficient had only dropped to 0.4, which should give the pressure pattern sufficient coherence to raise waves. But because of its high progression velocity, the oscillatory pressure pattern could feed energy only to waves which travel obliquely to the direction of mean air flow, with resonance occurring when the angle between the direction of propagation of the waves and the

wind direction is given to  $\cos\alpha = \frac{c}{u_p}$  (Phillips, 1957). This requires angles between wave crest and wind direction measurements in this study of between 0 and 10°, which were not observed. Even the smallest capillary ripples of wave length about 0.5 cm have a phase velocity of only 30 cm/sec, and thus, for the lowest air velocity at which waves were observed (critical fetch at  $x = 4.88$  meters,  $u_\infty = 3.2 \text{ m-sec}^{-1}$ ) one should have found the smallest value  $\alpha = 78^\circ$ .

The experimental results describing the nature of the origin of the first wind waves thus do not lead to an explanation by applying the existing theory.

#### 4.3 Shearing Flow Instability

Once the initial disturbances exist, regardless of their origins, energy can be transferred to them by the viscous mechanism described by Benjamin (1959) and Miles (1962a). Assuming that this mechanism controls further growth of the first wavelets, it will be active at all fetches in the first two stages of growth as we have defined them, and to some extent also in the third stage.

The experimental results describing the nature of the origin of the first wind waves thus do not lead to an explanation by applying the existing theory.

The analytical solution of Miles (1962a) applies to conditions of a logarithmic distribution of air velocity that does not change with fetch. Furthermore, no mean velocity gradient is accounted for in the water. The waves of wave number  $k$  are assumed infinitesimal in amplitude,  $a$ , ( $ak \ll 1$ ), and the critical layer where  $u(y) = c$  is presumed to be within the viscous sublayer of the air flow.

In analytical terms, the requirement for applicability of Miles' model is:

$$c_0 < 2.3 \left( u_* / \nu_a k \right)^{1/3} u_*, \quad (11)$$

where the phase speed is

$$c_0 = \left[ \frac{g}{k} + \frac{k \nu}{\rho_w} \right]^{1/2} \quad (12)$$

Here  $\gamma$  is the surface tension between air and water. These restrictions, with the exception of zero velocity in the water, were fulfilled in our experiments involving the high wind speed within the first 50 cm downstream of the plate, and in the case of the low wind speeds, for considerable distance upstream and downstream of the critical fetch.

The linearized stability theory of Benjamin and Miles estimates the development of small disturbances of the type

$$\eta = a_0 e^{ik(x-ct)} \quad (13)$$

where  $\eta$  is the water surface displacement,  $a_0$  is the amplitude of the initial disturbance of wave number  $k$ , and  $c$  is the complex phase speed given as

$$c = c_0 + ic_i \quad (14)$$

Disturbances will grow if the imaginary part  $c_i$  is positive. The net amplification factor  $m = kc_i$  consists of a sum of two terms: a growth rate  $m_a$  due to the Miles-Benjamin mechanism, and a damping rate  $m_w$  resulting from viscous dissipation of wave energy in the water. From the theory of small amplitude waves,

$$m_w = -2k^2 \nu_w - (2k^3 \nu_w c_0)^{1/2} e^{-2kd} \quad (15)$$

where  $d$  is the water depth,  $\nu_w$  is the kinematic viscosity of the water. The phase speed of the infinitesimal waves,  $c_0$ , is assumed unaffected by the process of energy transfer from the air to the water. The growth factor is determined from a solution of the viscous Orr-Sommerfeld equation as (Miles, 1962a):

$$m_a = \frac{1}{2} \left( \frac{\rho_a}{\rho_w} \right) U_0' \int_{c=c_0} \frac{w_i - \mathcal{F}_i - k \delta^* (w_r - \mathcal{F}_r) \mathcal{H}_i}{|\mathcal{F} - w|^2} \quad (16)$$

where  $\mathcal{F}$  and  $\mathcal{H}$  are complex functions of the variable

$$\mathcal{Z} = c / U_0' \delta^* \quad (17)$$

and  $w$  is a complex function discussed by Miles (1962b).

Since it is assumed that the velocity profile nearest the water is linear,  $U_o'$ , the slope of the mean wind profile at the surface is given by

$$U_o' \approx u_*^2 / \nu_a$$

The parameter  $\delta^*$  is given by  $(\nu_a / U_o' k)^{1/3}$ . In Miles' (1962a) approximations,  $w_i = 0$  so that

$$|f - w|^2 = (f_r - w_r)^2 + f_i^2 \quad (18)$$

In our calculations for  $m_a$ ,  $f_r$ ,  $f_i$  and  $H_i$  were determined from curves given in Fig. 3 of Miles' (1962a) paper. The  $w$  function was estimated from Miles (1962b) where

$$w = \frac{K C_o}{u_*} W(R, A)$$

$$R = \frac{K u_*}{k \nu_a}, \quad \text{and} \quad A = \frac{K (u_* - C_o)}{u_*}$$

The velocity  $u_1$  at the edge of the viscous sublayer,  $y = y_1$ , is found from the condition that the logarithmic law in the form given by Miles (1962a),

$$u(y) = u_1 + \frac{u_*}{K} \left[ \ln \left( \frac{4 K u_* y}{\nu_a} \right) - 1 + o(y/y_1) \right] \quad (19)$$

must asymptotically become identical to Eq. (2) for large values of  $y$ . With the term  $o[y_1/y] \approx 0$  in Miles' equations, it follows that

$$\frac{u_1}{u_*} \approx 6.9 \quad (20)$$

This value is within the range of 5.6 to 8 used in Miles' calculations.

From the above equations, the theoretical amplification factors  $m_a$  and  $m_w$  were calculated for the experimental conditions of this study. We note, of course, that the assumption, Eq. (13), applies to the wave component corresponding to the peak of the spectrum; i.e., the dominant wave. To extend the results to the whole spectrum



would require superposition of solutions, which is possible in principle because of the linearity of the model. However, we will concentrate primarily on the development of this component since it is defined best by the spectral data. The results for spatial growth of the dominant waves have already been introduced in Fig. 13. To compare the theoretical growth rates with time of any spectral component considered with the experimental results we have used a transformation (Gaster, 1962) to give the theoretical slope

$$S_T = \frac{\partial \ln \phi(n)}{\partial x} = \frac{2m}{c_g} \quad (21)$$

where  $m = m_a + m_w$  from Eq. (15) and (16), and  $c_g$  is the group velocity:

$$c_g = c_o \left[ 1 - \frac{1}{2} \left( \frac{\rho_w - k^2 \nu}{\rho_w + k^2 \nu} \right) \right], \quad (22)$$

where  $\rho_w$  is the water density.

The theoretical slope  $S_T$  then can be compared with the slope  $S_E$  obtained from experimental data.  $S_E$  was determined as the slope of the best fitting straight line of passing through a plot of  $\log \phi(n)$  vs.  $x$ . This slope is equal to twice the growth rate of the wave amplitude, since the spectrum corresponds to the wave amplitude squared. A comparison of data based on theory and experiment is given in Table 4. These results indicate fractional differences of 61% or less between theory and experiment for growth of the dominant waves in second stage of development. In two of the four cases listed this error is outside the estimated uncertainty in evaluating the slope  $S_E$ .

All of the data listed in Table 4 coincided with Miles' (1962a) additional restriction that the ratio  $[(\rho_a/\rho_w) u_*^2 / \nu_a k] < c_o$ . When these two velocity scales become the same order, the growth rates of small waves may be modified by the Kelvin-Helmholtz class of instability.

Because of the sharpness of the spectral peaks, caution has to be used in interpreting the growth of Fourier components on either side of the spectral peak. However, it is useful for a qualitative comparison to examine the experimental slope along with the

Table 4

Comparison between Experimental Growth of Dominant Wave with Fetch  
and Miles' Theoretical Predictions Assuming  $u_1 = 6.9 u_*$

$u_*$ (cm-sec <sup>-1</sup> )	$n_{\max}$ (Hz)	$k$ (cm <sup>-1</sup> )	$c_0$ (cm-sec <sup>-1</sup> )	$\frac{\rho_a u_*^2}{\rho_w a k}$ (cm-sec <sup>-1</sup> )	$z$	$m_a$ (sec <sup>-1</sup> )	$-m_w$ (sec <sup>-1</sup> )	$\frac{2mx}{c_g}$	$S_T$ (m <sup>-1</sup> )	$S_E$ (m <sup>-1</sup> )	% Diff. $\frac{(S_T - S_E)}{S_E} 100$
15.8	7.0	1.64	26.7	0.84	0.451	0.241	0.054	13.4	2.1	1.3 ± 0.4	+61
17.0	7.5	1.82	25.9	0.87	0.417	0.354	0.0066	15.4	3.1	3.7 ± 0.8	-16
19.0	8.5	2.16	24.7	0.91	0.362	.497	.0933	21	4.3	6.5 ± 0.6	-34
35.0	11.0	2.96	23.4	2.54	0.167	2.57	0.175	2.18	24.	25. ± 1	-4.0

theoretical values over a range of wave number. As an illustration of the distribution of the amplification factor in terms of the Slope  $S$ , theoretical experimental results for  $u_* = 19 \text{ cm-sec}^{-1}$  are plotted together in Fig. 16.

The influence of the surface current. One potentially serious limitation of Miles' theory is the disregard for the shearing current that develops in the water. Taking this motion into account might improve the predictions of the two dimensional theory for shearing flow instability.

Since our measurements are taken at a fixed location, two possible effects of the current may enter into the comparison between theory and experiment. The first involves accounting for a shift resulting from finite surface velocity,  $u_s$ , on the transformation between wave number and frequency. The second influence may stem from the fact that the gradients in the drift current in the thin viscous layer at the water surface may modify the growth rates as well as the dissipation rates. An increase in amplitude may be expected by increased energy transfer to the water associated with the surface current, as has been illustrated by Tominaga (1964) for the case of waves on a current of uniform velocity. This is only partially compensated for by modification of the dissipation rate.

To examine the importance of the drift current on our wave measurements, we looked at instability theories that attempted to incorporate such an effect. Miles' mechanism has been applied to superimposed liquids with linear velocity profiles by Feldman (1957) and Miles (1960). However, these theories differ from our laboratory condition in the assumption of the location of the critical layer. In Miles and Feldman's models, this layer was supposed to exist in the lower, heavier fluid.

A model in which the critical layer lies in the air and in which velocity gradients exist in both fluids has been considered

for gas flow over thin liquid layer by Cohen and Hanratty (1965). However, a newer theory for deeper liquid layers has been reported by Drake (1967), and Drake and Plate (1968). This model is adopted here to predict the behavior of waves in the second stage of growth. The application of this model requires that the water surface velocity be known in addition to the parameters of Miles' model for which we used the experimental results reproduced in Fig. 14.

Drake's model assumes a mean velocity distribution which is identical in the air to that of Miles (1962a) with the exception of accounting for translation due to the surface velocity. To specify the water current, a linear profile in the thin layer near the water surface is assumed which abruptly changes with depth into a logarithmic profile fixed at the bottom of the channel. For deep water waves, the contribution from the logarithmic portion of the current profile to energy transfer becomes unimportant. Thus the linear profile, which originally was developed for instabilities of small disturbances on a moving stream, can be applied readily to wave growth in the case of a closed circulation induced in water standing in the channel. To a first approximation, the following equation for the phase speed,  $c_r - u_s$ , relative to the surface velocity is found (Drake, 1967):

$$(c_r - u_s)^2 + \frac{u_*^2 \rho_a}{\mu_w k} (c_r - u_s) - c_o^2 \approx 0 \quad (23)$$

where  $\mu_w$  is the viscosity of water.

To higher approximations, the right side of Eq. (23) is equal to the complex function  $u_*^2 Q$  where  $Q$  is given by

$$Q = \frac{G_w + G_a}{1 + F_w + F_a} \quad (24)$$

In this equation, the functions with subscript w stem from the water solutions, while  $G_a$  and  $F_a$  result from analysis of the air motion.

These functions are given by Drake and Plate (1968) in terms of  $c_r$ ,  $u_*$  and  $u_s$ . A solution for Eq. (23) and (24) is obtained iteratively by assuming first  $Q = 0$ , calculating  $c_r$  from Eq. (24)

and inserting this value into the terms for the functions  $G$  and  $F$  in Eq. (24), from which a new estimate for  $Q$  is found. The new approximation for  $Q$  results in a revised complex phase velocity  $c = \alpha_s$ . The iteration is repeated until a constant value of  $c$  is attained whose imaginary part is converted into the spatial growth rate by means of Eq. (21) from the time growth rates  $m = kc_i$ , with  $c$  given by Eq. (23).

For the spectral wave peaks observed at low shearing velocities, calculations of the growth rates in terms of  $S_T$  from Drake's model are compared with experimental results in Table 5. For these calculations,  $\alpha_s$  was taken as  $\alpha_s = 0.026 \alpha_m$ . Evidently, the incorporation of the influence of the drift current slightly improved the agreement between theory and experiment, particularly in the  $u_* = 19$  cm-sec<sup>-1</sup> case, for the dominant waves in stage two of growth.

To illustrate differences and similarities of Drake's and Miles' models, the case of  $u_* = 19$  cm/sec was used again as is shown in Fig. 16. At low wave numbers,  $k < 1$  cm<sup>-1</sup>, both models give essentially the same results for  $S$ . For larger wave numbers, however, Miles' theory predicts lower growth rates than Drake's model with a maximum at  $k \approx 2.3$  cm<sup>-1</sup>. On the other hand, Drake's model shows a nearly constant rate of growth with fetch beyond a wave number of about 3 cm<sup>-1</sup>.

Qualitative comparison between the growth rates estimated experimentally from the spectral densities suggests that Miles' model comes more closely to predicting the shape of the curve of  $S_E(k)$ . But the maximum growth given by his theory is systematically too low compared with this particular case. Miles' theory actually yields the decrease with decreasing wind speed in frequency for the wave of maximum growth, as observed. However, in all cases listed in Table 3, his model tends to overestimate the frequency for the dominant wave in contrast to our experimental results for the second stage of growth. According to Drake's calculations, the principal influence of the drift current on growth rates at low surface velocities lies in the range of wave numbers higher than 1 cm<sup>-1</sup> for the case in Fig. 16.

Table 5

Comparison between Experimental Growth of Dominant Wave with Fetch and Drake's Theory Accounting for the Effect of the Drift Current  $u_1 = 6.9 u_*$

$u_*$ (cm-sec <sup>-1</sup> )	$u_s$ (cm-sec <sup>-1</sup> )	$n_{\max}$ (Hz)	$k$ (corr.) (cm <sup>-1</sup> )	$S_T$ (m <sup>-1</sup> )	$S_E$ (m <sup>-1</sup> )	$\frac{(S_T - S_E)}{S_E} 100$
15.8	8.90	7.0	1.36	2.0	$1.3 \pm 0.4$	+54
17.0	9.75	7.5	1.59	3.1	$3.7 \pm 0.8$	-16
19.0	10.7	8.5	1.91	5.1	$6.5 \pm 0.6$	-22

In this range, growth rates are increased substantially by energy exchange from the water current combined with modification of the viscous dissipation.

Acknowledgements. We are indebted to Charles Liu, Peter Soo, J. R. Lai, and R. Biro for the assistance in data processing. The helpful comments of J. W. Deardorff in revising the original manuscript are greatly appreciated. Thanks go to Colorado State University for the use of the wind-water tunnel. This work was sponsored by the National Science Foundation in connection with its contract with the National Center for Atmospheric Research, and its grant No. GK 188 to Colorado State University.

## CAPTION LIST

### Figures

Fig. 1. Schematic diagram of the experimental arrangement of combined air and water flow.

Fig. 2. Photographs of reflections of the capacitance gauge wire on the water surface. Scale is shown in inches.

Fig. 3. Distribution of average air velocity in the downstream direction at various fetches, with and without inlet grid.

Fig. 4. Distribution of intensities in longitudinal component of the air flow. a. for  $u_* = 45 \text{ cm-sec}^{-1}$  at different fetches. b. for  $u_* = 19 \text{ cm-sec}^{-1}$  (without grid), and  $u_* = 15.8 \text{ cm-sec}^{-1}$  with grid) at  $x = 488 \text{ cm}$ . Curves of Laufer (1954) and Klebanoff (1954) are added for comparison. Laufer's results correspond to fully developed pipe flow with Reynolds number based on pipe diameter  $D$ .

Fig. 5. Spectra of air turbulence at critical fetch of  $x = 350 \text{ cm}$ . with  $u_* = 17 \text{ cm-sec}^{-1}$  (without grid), and  $u_* = 15.8 \text{ cm-sec}^{-1}$  with grid.

Fig. 6. Distribution with height of the apparent rate of dissipation for air flow over small waves.

Fig. 7. Non-dimensional spectra of turbulence in longitudinal component of air flow. a.  $u_* = 45 \text{ cm-sec}^{-1}$  for typical heights and fetches. b.  $u_* = 19 \text{ cm-sec}^{-1}$  (without grid) at  $x = 488 \text{ cm}$ . c.  $u_* = 15.8 \text{ cm-sec}^{-1}$  (with grid).

Fig. 8. Photographs of the onset of visible surface waves at the critical wind speed with inlet grid for fetch  $x = 3.5 \text{ m}$ . The



ruler measures distance  $x$  in inches. Three quarter views down tunnel: a. just below critical speed,  $u_{\infty} = 2.9 \text{ m-sec}^{-1}$ . b. just above critical speed,  $u_{\infty} = 3.1 \text{ m-sec}^{-1}$ . c. at higher wind speed,  $u_{\infty} = 3.4 \text{ m-sec}^{-1}$ . d. still higher wind speed,  $u_{\infty} = 4.2 \text{ m-sec}^{-1}$ . Views from side of tunnel: e.  $u_{\infty} = 3.8 \text{ m-sec}^{-1}$ . f.  $u_{\infty} = 4.3 \text{ m-sec}^{-1}$ . g.  $u_{\infty} = 5.3 \text{ m-sec}^{-1}$ . h.  $u_{\infty} = 7.5 \text{ m-sec}^{-1}$ .

Fig. 9. Photograph of waves on the water taken near the trailing edge of the aluminum plate for  $u_{*} = 35 \text{ cm-sec}^{-1}$ .

Fig. 10. Typical recordings of capacitance gauge response near critical wind speed (with grid). Data shown are for different wind speeds at  $x = 3.50$  meters. a. Records taken at high sensitivity of the wave gauge below critical wind speed. b. Records similar to those in a, but taken at much lower sensitivity, beyond wind speed.

Fig. 11. Amplitude spectra for wavelets being generated at low wind speeds. These records indicate the evolution of the spectra with fetch in the region  $x = 488 \text{ cm}$ , for  $u_{*} = 19 \text{ cm-sec}^{-1}$ .

Fig. 12. Amplitude spectra for the waves developing downstream of the plate.  $u_{*A} = 35 \text{ cm-sec}^{-1}$ .

Fig. 13. Growth with fetch of single components of the wave spectrum for  $u_{*A} = 35 \text{ cm-sec}^{-1}$ , and  $u_{*A} = 19 \text{ cm-sec}^{-1}$ . Wave components shown are for the spectral peak, whose frequency is  $n_{\text{max}}$ .

Fig. 14. Typical distributions with fetch of drift velocity of the water surface.

Fig. 15. Space-time correlations for the longitudinal component of air turbulence, where  $u_{*} = 35 \text{ cm-sec}^{-1}$ , and the distance above the mean water level is  $y = 2.5 \text{ cm}$ .

Fig. 16. Comparison between experimental results and Miles' (1962) theory, with Drake's (1967) theory correcting for the drift current. The wave number for the experimental data has been modified for water surface speed by Eq. (23).

### Tables

Table 1. Characteristic properties of the turbulence in air flowing over small waves.

Table 2. Variation in frequency of the spectral peak with wind speed in the second stage of wave growth.

Table 3. Increase in frequency of spectral peak with wind speed in the second stage of growth.

Table 4. Comparison between experimental growth of dominant wave with fetch and Miles' theoretical predictions assuming  $u_1 = 6.9 u_{*}$ .

Table 5. Comparison between experimental growth of dominant wave with fetch and Drake's theory accounting for the effect of the drift current  $u_1 = 6.9 u_{*}$ .

## APPENDIX

In this additional note, an argument is outlined which demonstrates that the maximum value of the spectral density for the peak frequency  $n_{\max}$  of a (gravity) wave spectrum should follow an  $n_{\max}^{-5}$  envelope curve. This is a direct consequence of (a) the similarity spectrum postulated by Hidy and Plate (1965), and (b) the assumption that the amplitude of the dominant wave is limited by the requirement that the acceleration of water particles at the wave crest cannot exceed the acceleration of gravity.

According to the findings of Hidy and Plate (1965), the shape of the wave spectrum is independent of peak frequency when written in the form

$$S(n/n_{\max}) = \phi(n) n_{\max} / \sigma^2, \quad (\text{A.1})$$

where  $S$  is the dimensionless spectral function, and  $\sigma^2$  is the variance of the water surface displacement.

Our observations of this study as well as those in Hidy and Plate (1966) have indicated that the wave spectrum is sufficiently sharply peaked that most of the energy in the spectrum has to be associated with the wave of dominant frequency,  $n_{\max}$ . As a first approximation, the <sup>spectral component of the dominant frequency</sup> ~~wavy surface~~ may be given by a sinusoidal function:

$$\eta \approx a_{\max} \cos(k_{\max} x - 2\pi n_{\max} t), \quad (\text{A.2})$$

where  $a_{\max}$  is the amplitude of the wave corresponding to  $n_{\max}$ , and  $\eta$  is the water surface displacement. Then

$$\sigma^2 = C \sigma_{\max}^2 \approx 0.5 C a_{\max}^2, \quad (\text{A.3})$$

which follows from the notion of the similarity spectrum.

The maximum amplitude  $a_e$  that the dominant wave can attain if gravity controls the wave dynamics is found by setting the maximum vertical acceleration equal to the gravitational acceleration, or

$$a_e (2\pi n_{\max})^2 = g. \quad (\text{A.4})$$

Thus  $a_e$  is related to  $a_{\max}$  such that  $a_{\max} (2\pi n_{\max})^2 = \alpha g$ , where  $\alpha$  is a constant less than unity.

We have found for the laboratory observations that the dimensionless spectrum is universal in shape so that

$$n_{max} \phi(n_{max}) = \sigma^2 S(1), \quad (A.5)$$

where  $S(1) \approx 0.4$  from Fig. 2 of Hidy and Plate (1965). Consequently, the combination of Eqs. (A.3) and (A.5) with (A.4) leads to the result that the envelope for  $(n_{max})$  at maximum wave amplitude is:

$$\phi(n_{max}) = \frac{0.2C}{(2\pi)^4} g^2 n_{max}^{-5} \quad (A.6)$$

Plate (1967) has shown that the dominant wave in a wind wave spectrum typically contains 50% of the total energy of the wave spectrum. Hence the constant C is expected to be the order of two. If (A.6) is compared with Eq. (9), and we identify  $0.2C/(2\pi)^4$  with Phillips' constant,  $\beta$ , we find  $\beta \approx 2.5 \times 10^{-4}$  instead of  $7.5 \times 10^{-6}$  based on a wide variety of water wave observations (Phillips, 1966). The result (A.6), of course, applies only to the behavior of the spectral density at the peak frequency, and is independent of the shape of the spectrum.

## REFERENCES

- Benjamin, T. B. 1959 J. Fluid Mech. 6, 161.
- Blackman, R. B. & J. W. Tukey 1958 Measurements of Power Spectra from the Point of View of Communications Engineering. New York: Dover, 189 p.
- Bradshaw, P. 1967 J. Fluid Mech. 27, 209.
- Clauser, F. 1956 "The turbulent boundary layer." Adv. Appl. Mech. 4. New York: Academic Press.
- Cohen, L. S. & T. J. Hanratty 1965 A.I.Ch.E. Journal 11, 138.
- Drake, R. 1967 The generation of wind waves on open channel flows. Unpublished Ph.D. dissertation, Colorado State University, Department of Civil Engineering, Fort Collins, Colorado, 154 p.
- Drake, R. & E. J. Plate 1968 The generation of wind waves on open channel flows. Proc. 10th Midwestern Mechanics Conference.
- Feldman, S. 1957 J. Fluid Mech. 2, 343.
- Gaster, M. 1962 J. Fluid Mech. 14, 222.
- Hess, G. D. 1968 Turbulent air flow over small water waves. Unpublished Ph.D. dissertation, University of Washington, Seattle, Washington.
- Hidy, G. M. & E. J. Plate 1965 Phys. of Fluids 8, 1387.
- Hidy, G. M. & E. J. Plate 1966 J. Fluid Mech. 26, 651.
- Hinze, J. O. 1959 Turbulence. New York: McGraw-Hill, 586 p.
- Keulegan, G. H. 1951 J. Natl. Bur. of Standards 46, 358.
- Klebanoff, P. S. 1954 NACA T.N. 3133.
- Laufer, J. 1954 NACA T.R. 1174.
- Miles, J. W. 1960 J. Fluid Mech. 8, 593.
- Miles, J. W. 1962a J. Fluid Mech. 13, 433.
- Miles, J. W. 1962b J. Fluid Mech. 13, 427.
- Phillips, O. M. 1957 J. Fluid Mech. 2, 417.

- Phillips, O. M. 1958 J. Fluid Mech. 4, 426.
- Phillips, O. M. 1966 The Dynamics of the Upper Ocean. Cambridge: Cambridge University Press, 261 p.
- Plate, E. J. 1965 La Houille Blanche No. 6, p. 597.
- Plate, E. J. 1967 ASCE Journal Hydraulics Div. 93, 310.
- Plate, E. J. & G. M. Hidy 1967 J. Geophys. Res. 72, 4627.
- Pond, S., R. W. Stewart & R. W. Burling 1963 J. Atmos. Sci. 20, 319.
- Sandborn, V. A. & R. D. Marshall 1965 Local isotropy in wind turbulence. TR CER-65 VAS-RDM-71, Civil Engineering Department, Colorado State University, Fort Collins, Colorado.
- Sutherland, A. 1967 Spectral measurements and growth of wind-generated water waves. TR 84, Department of Civil Engineering, Stanford University, Stanford, California.
- Tominaga, M. 1964 Bull. de Soc. Franco-Japonaise d'Océanographie 2, No. 1, 22.
- Willmarth, W. & C. Wooldridge 1962 J. Fluid Mech. 14, 187.

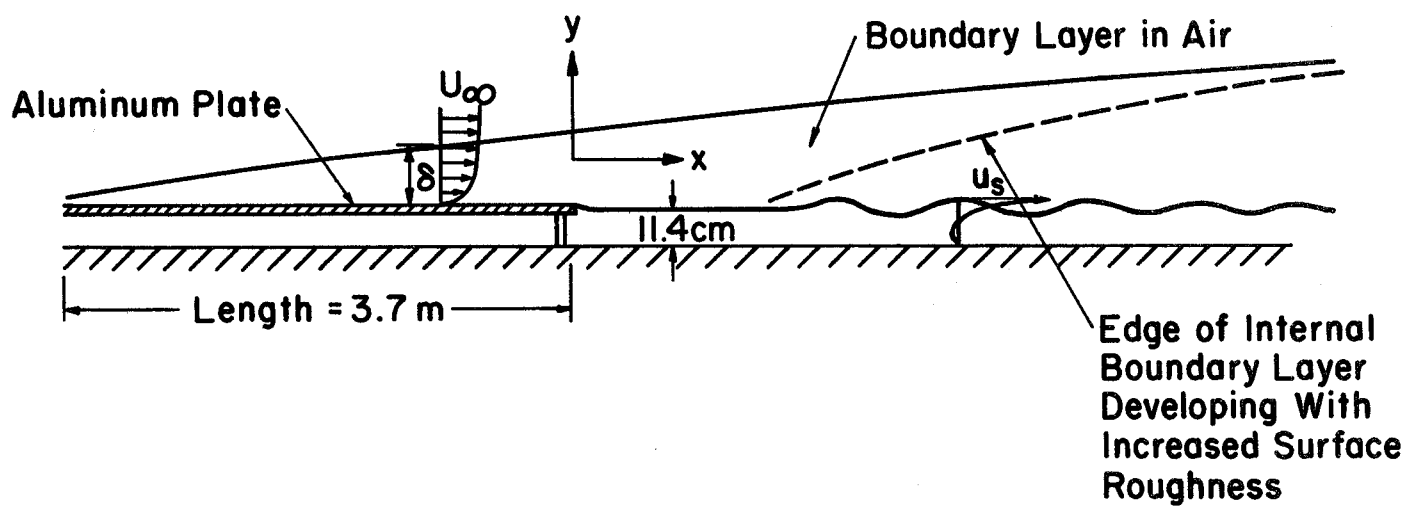
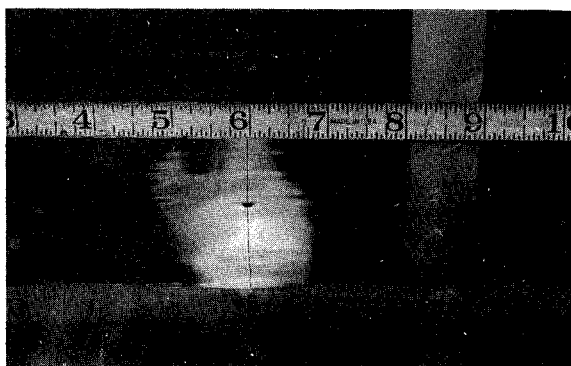
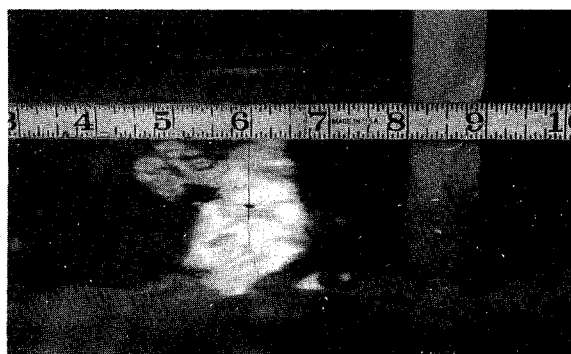


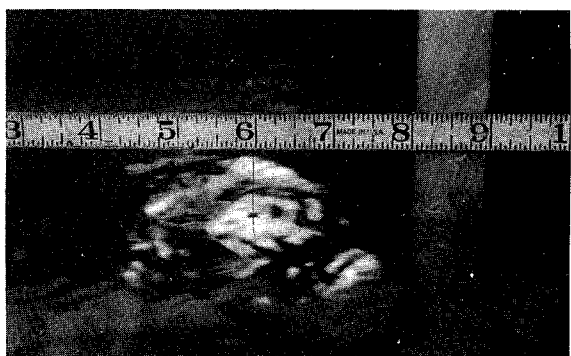
Figure 1



a.



b.



c.

Figure 2



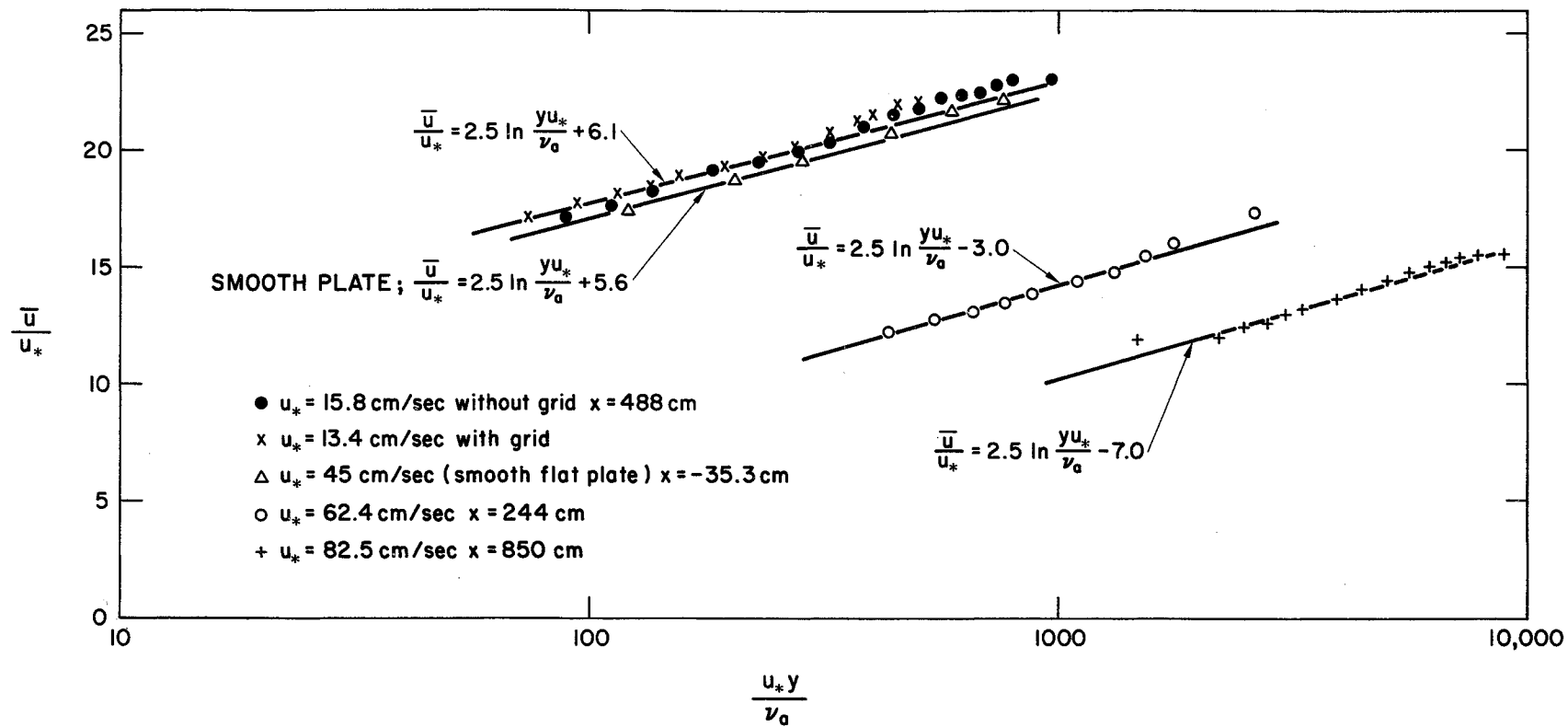


Figure 3

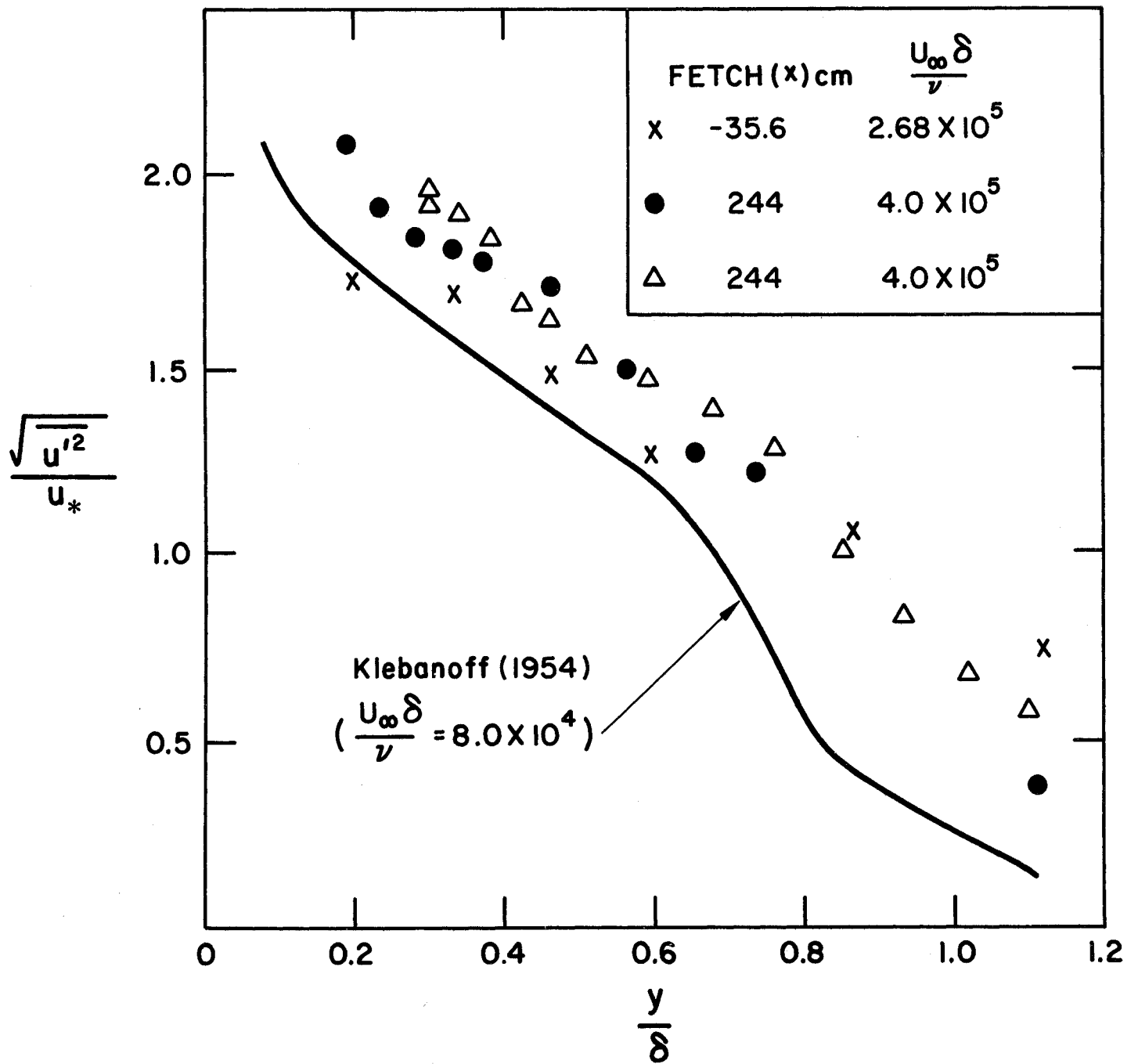


Figure 4-a

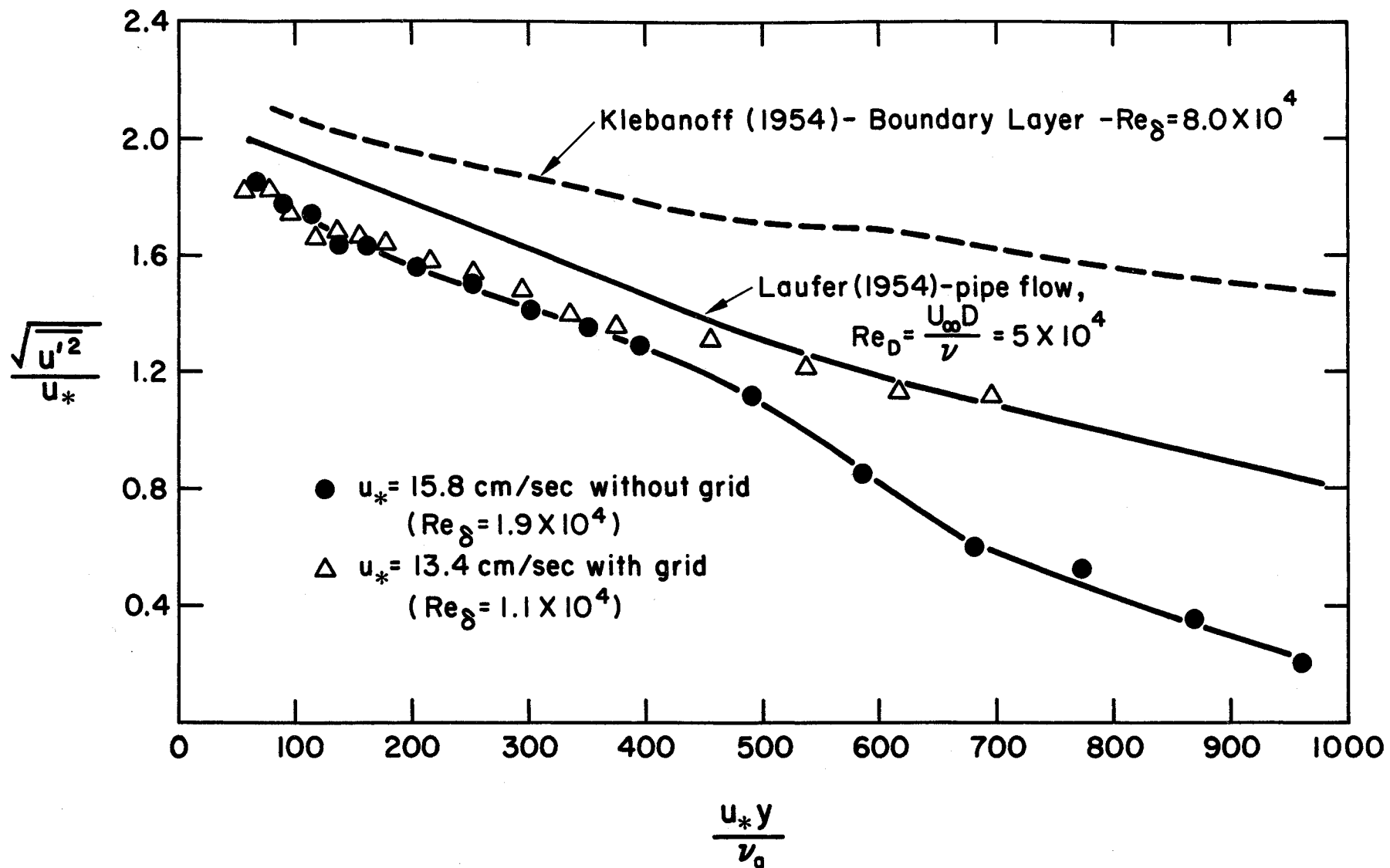


Figure 4-b

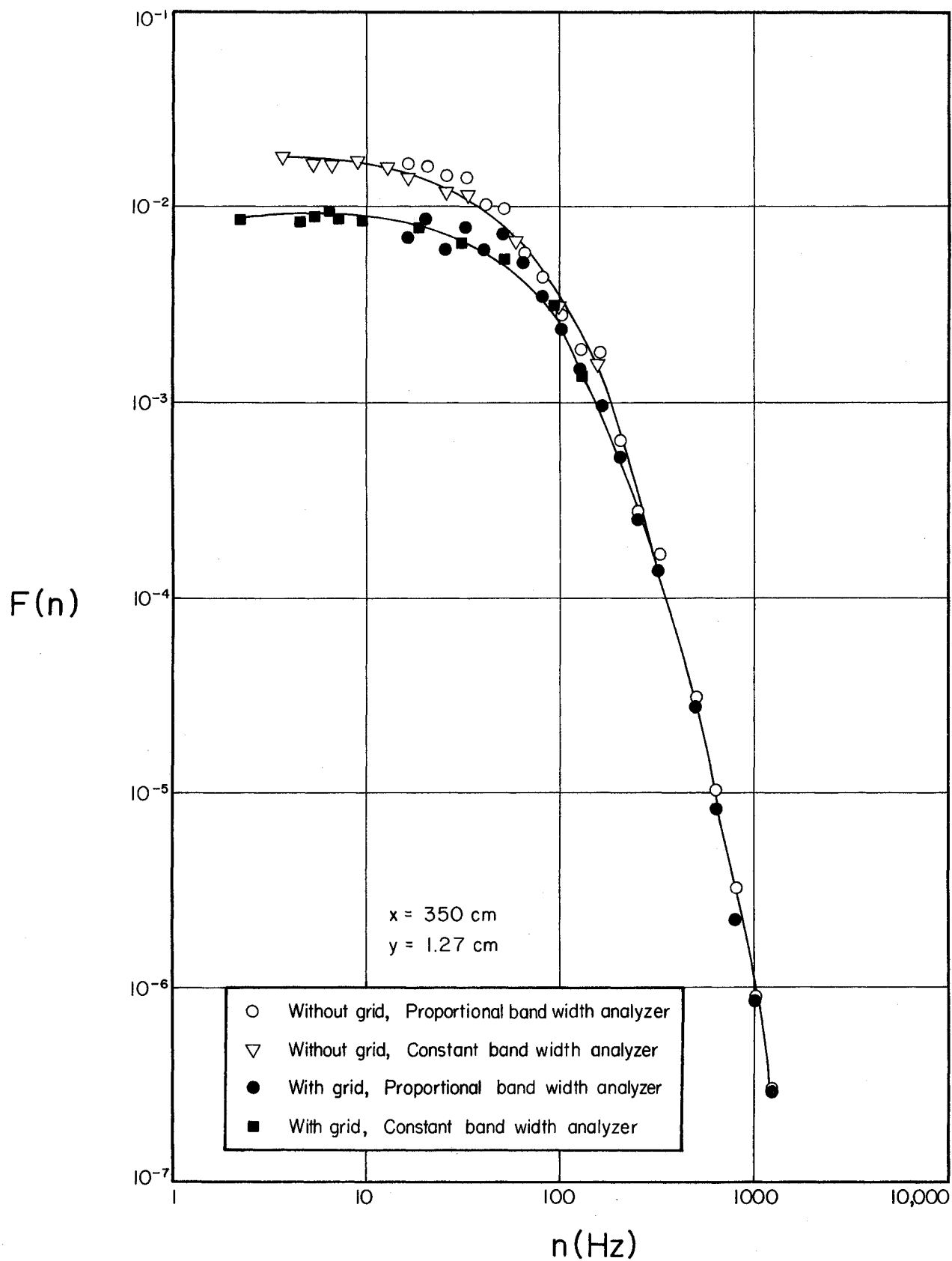


Figure 5

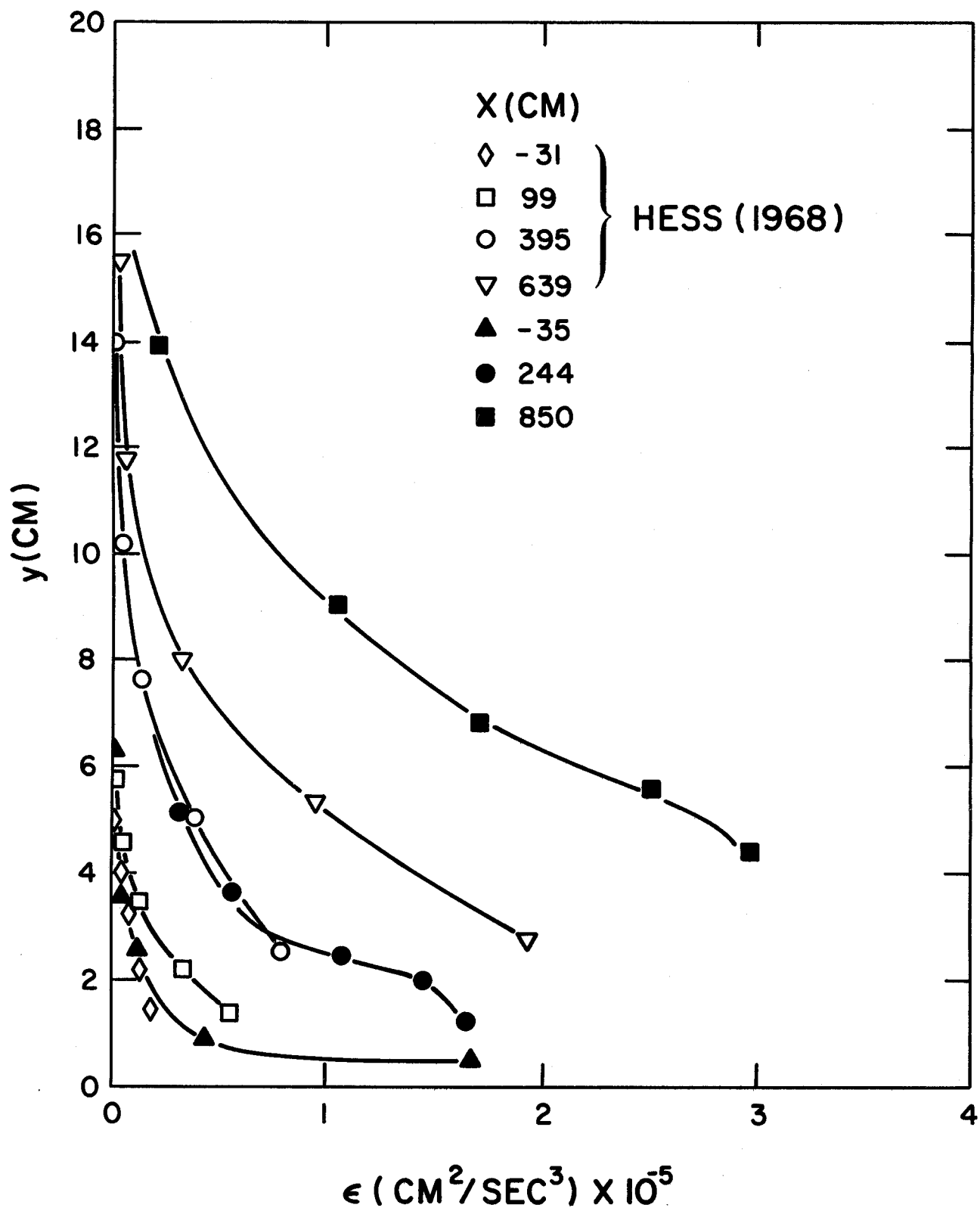


Figure 6

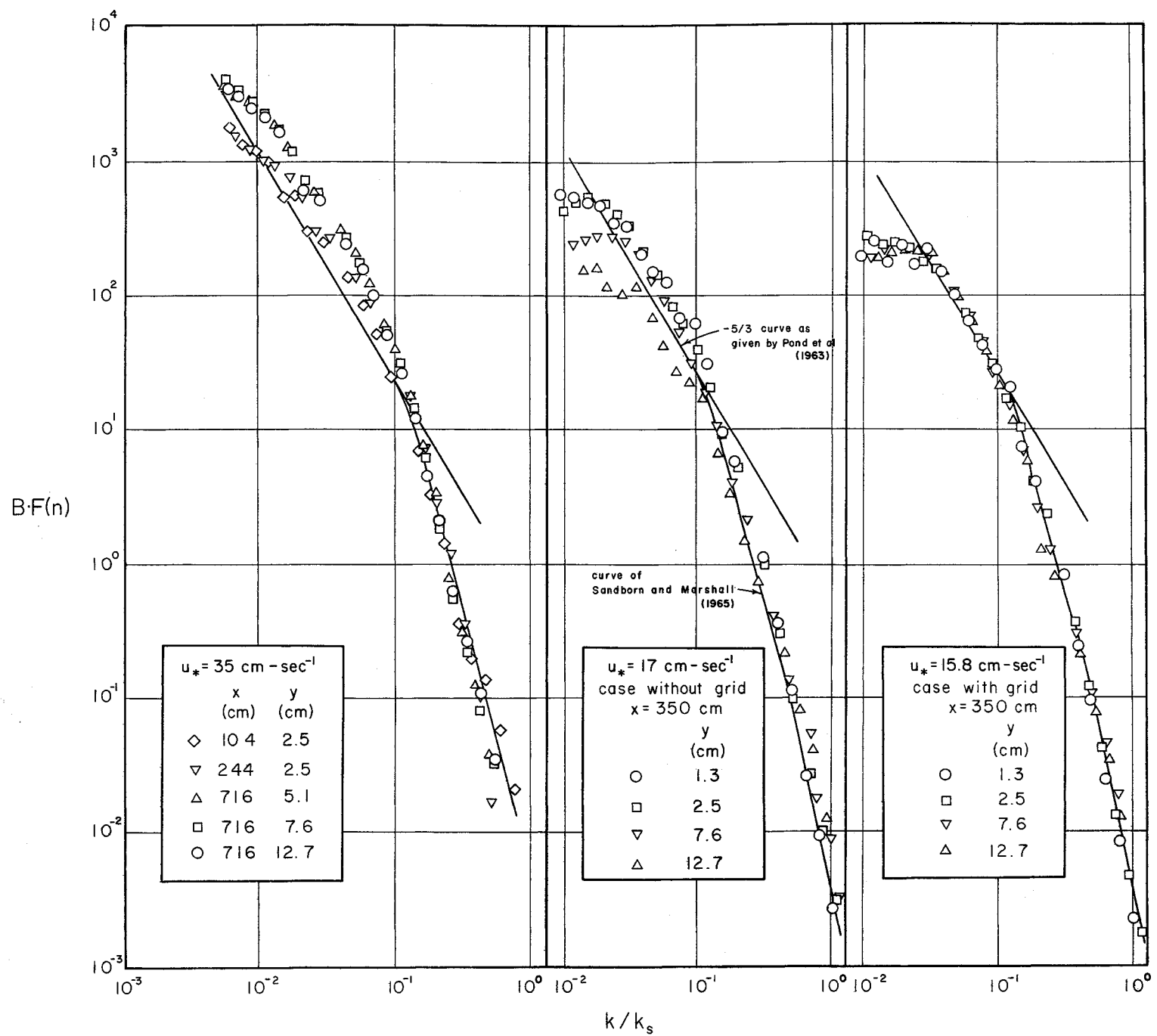
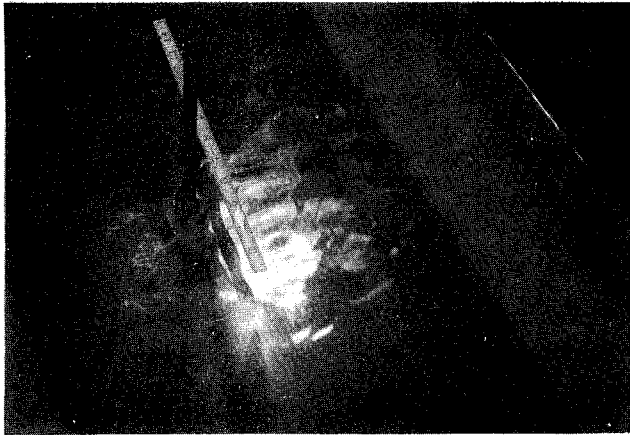
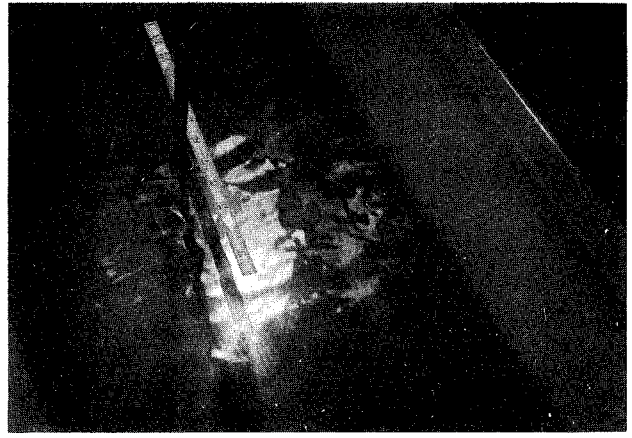


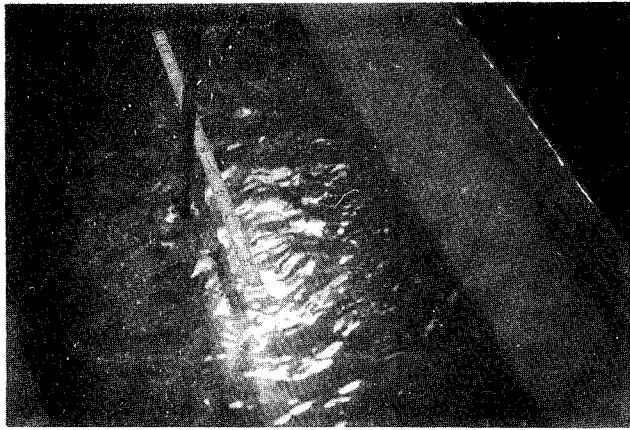
Figure 7



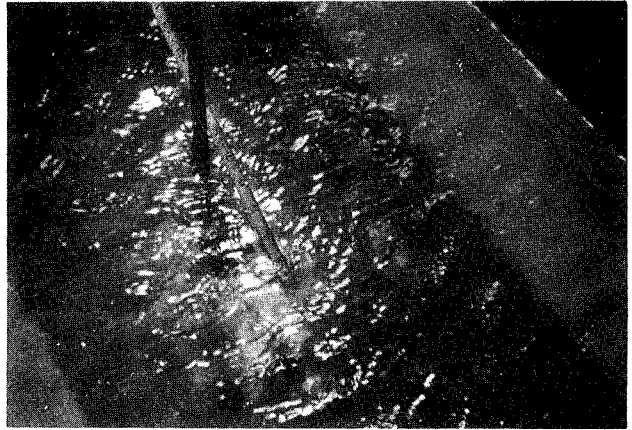
a



b



c



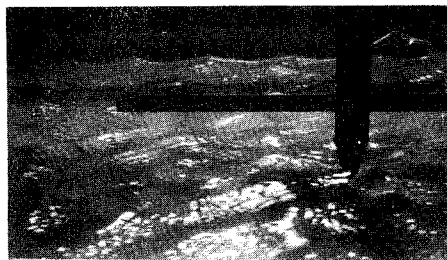
d



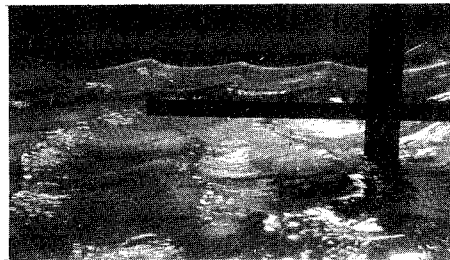
e



f



g



h

Figure 8

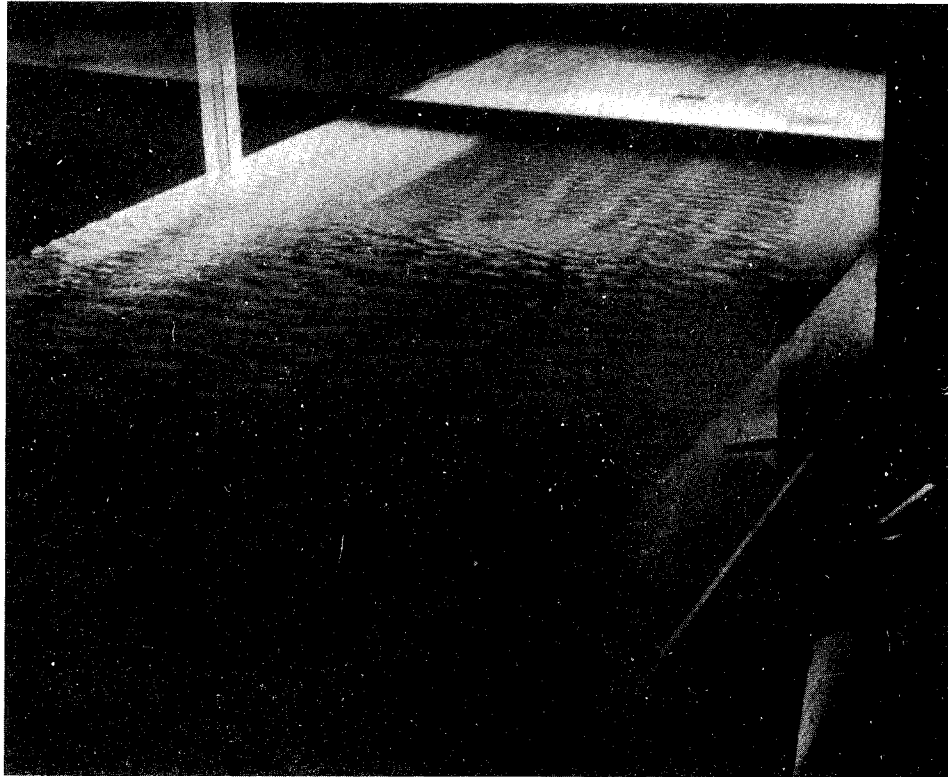


Figure 9



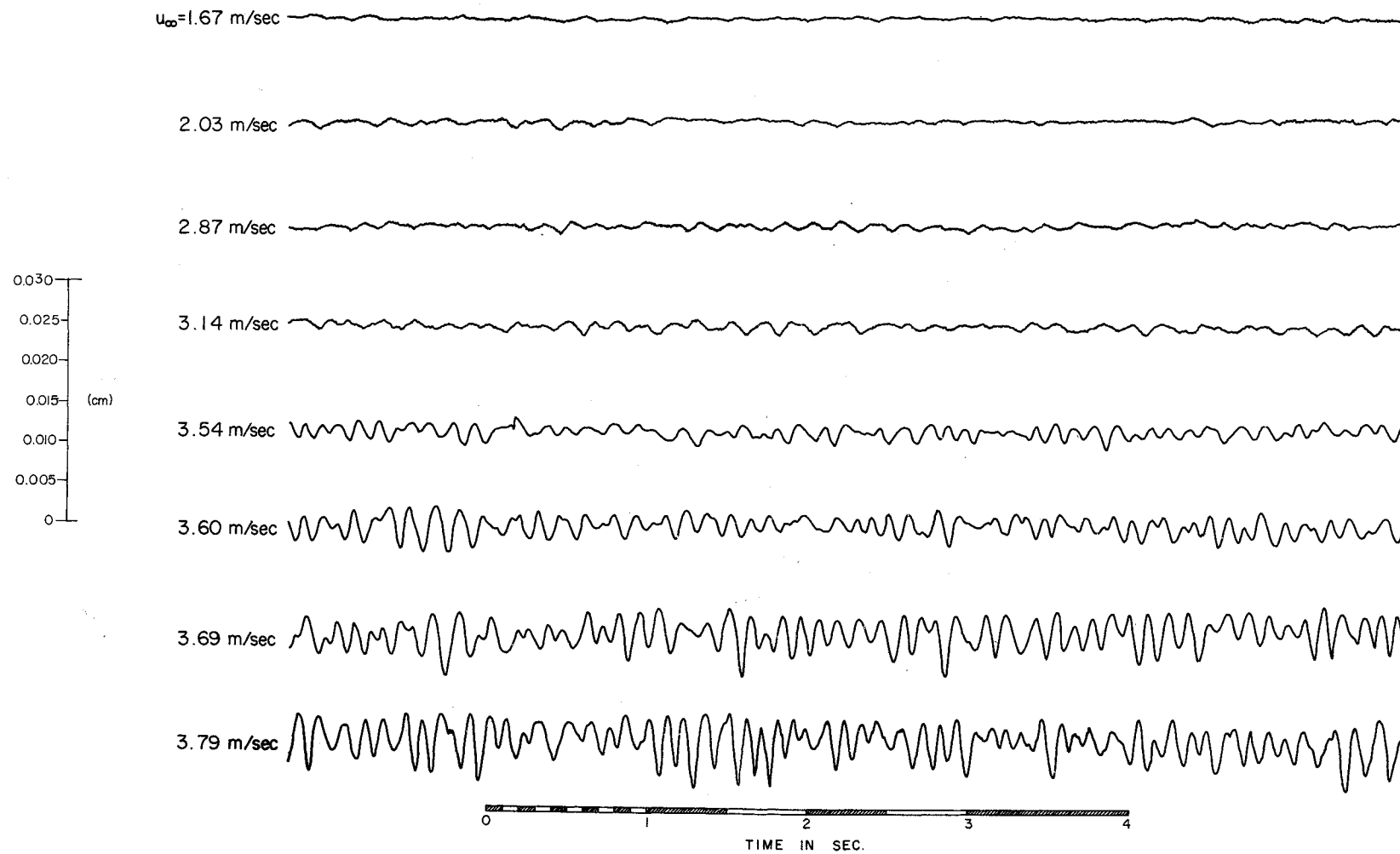


Figure 10-a

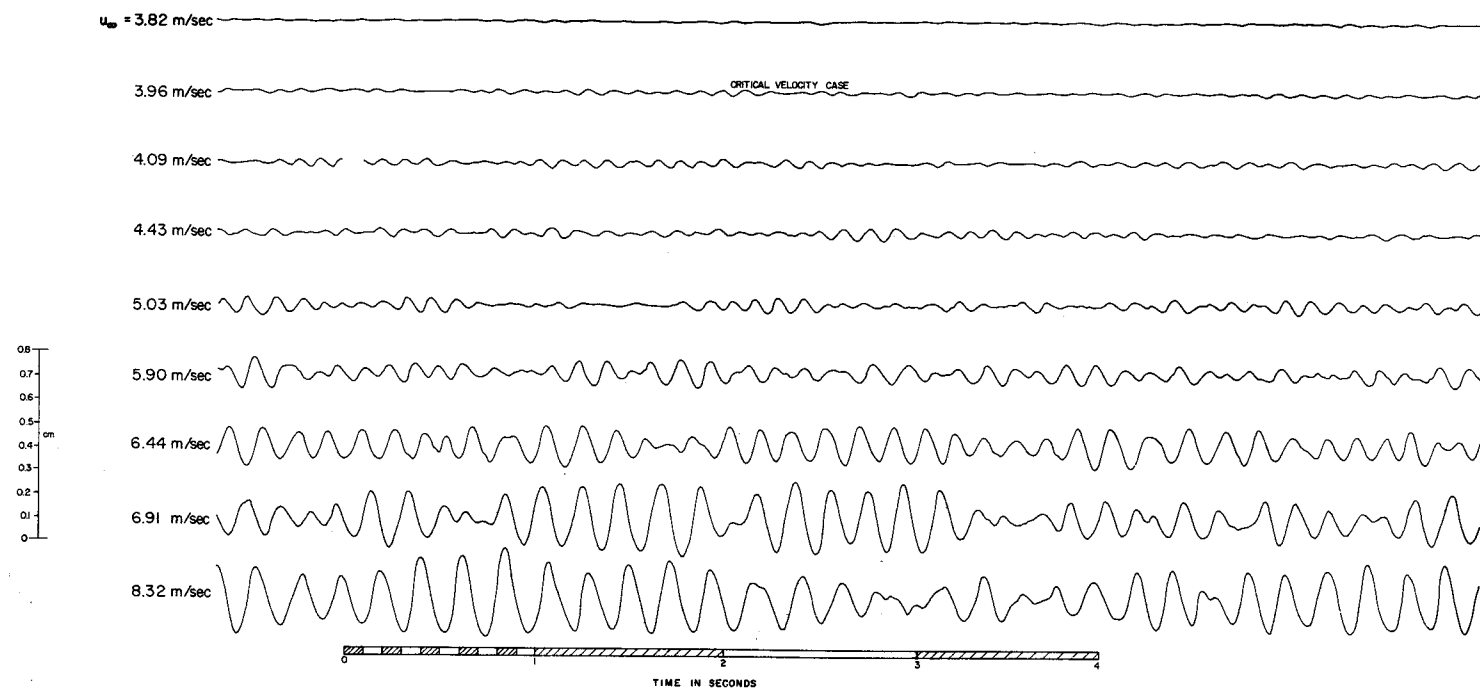


Figure 10-b

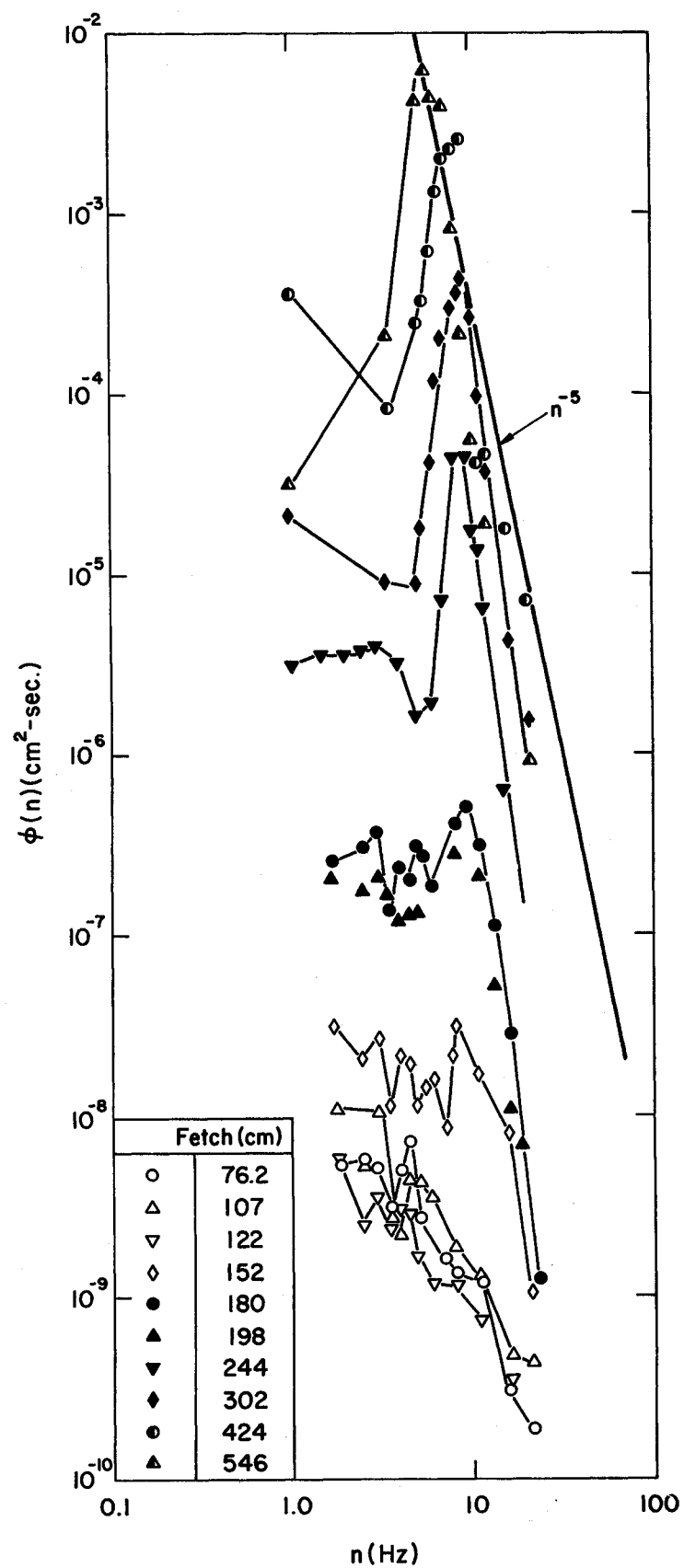


Figure 11

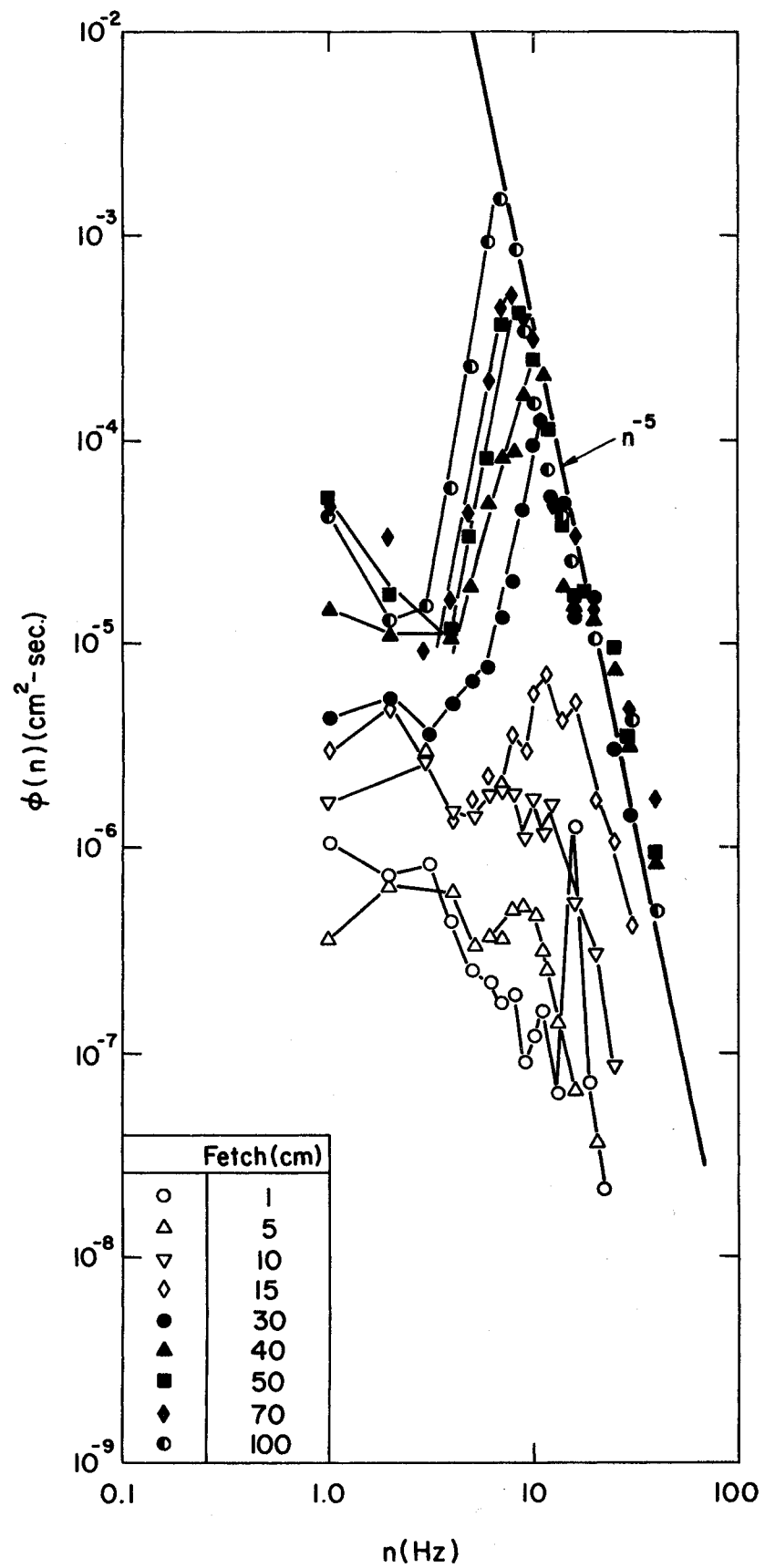


Figure 12

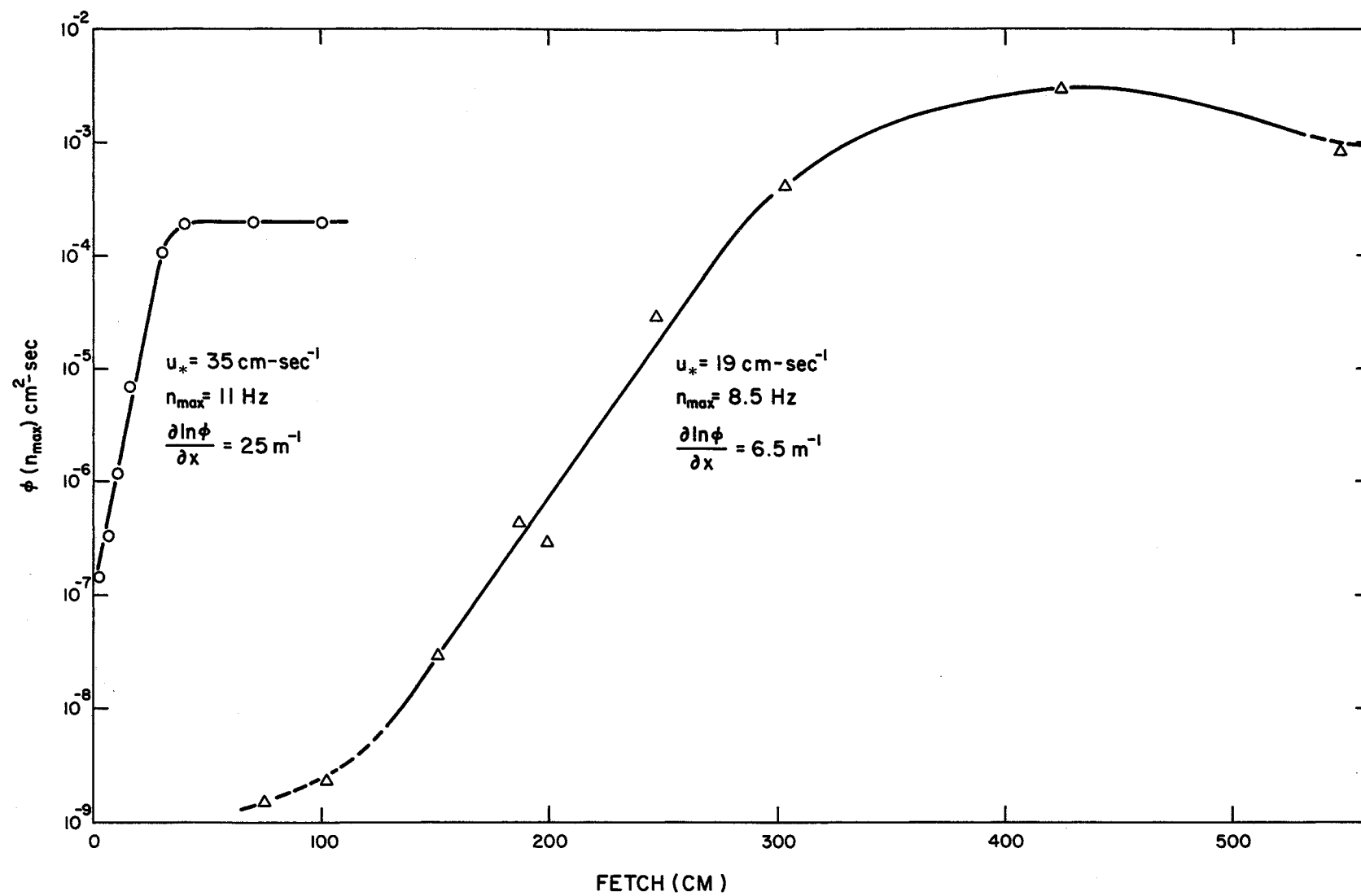


Figure 13

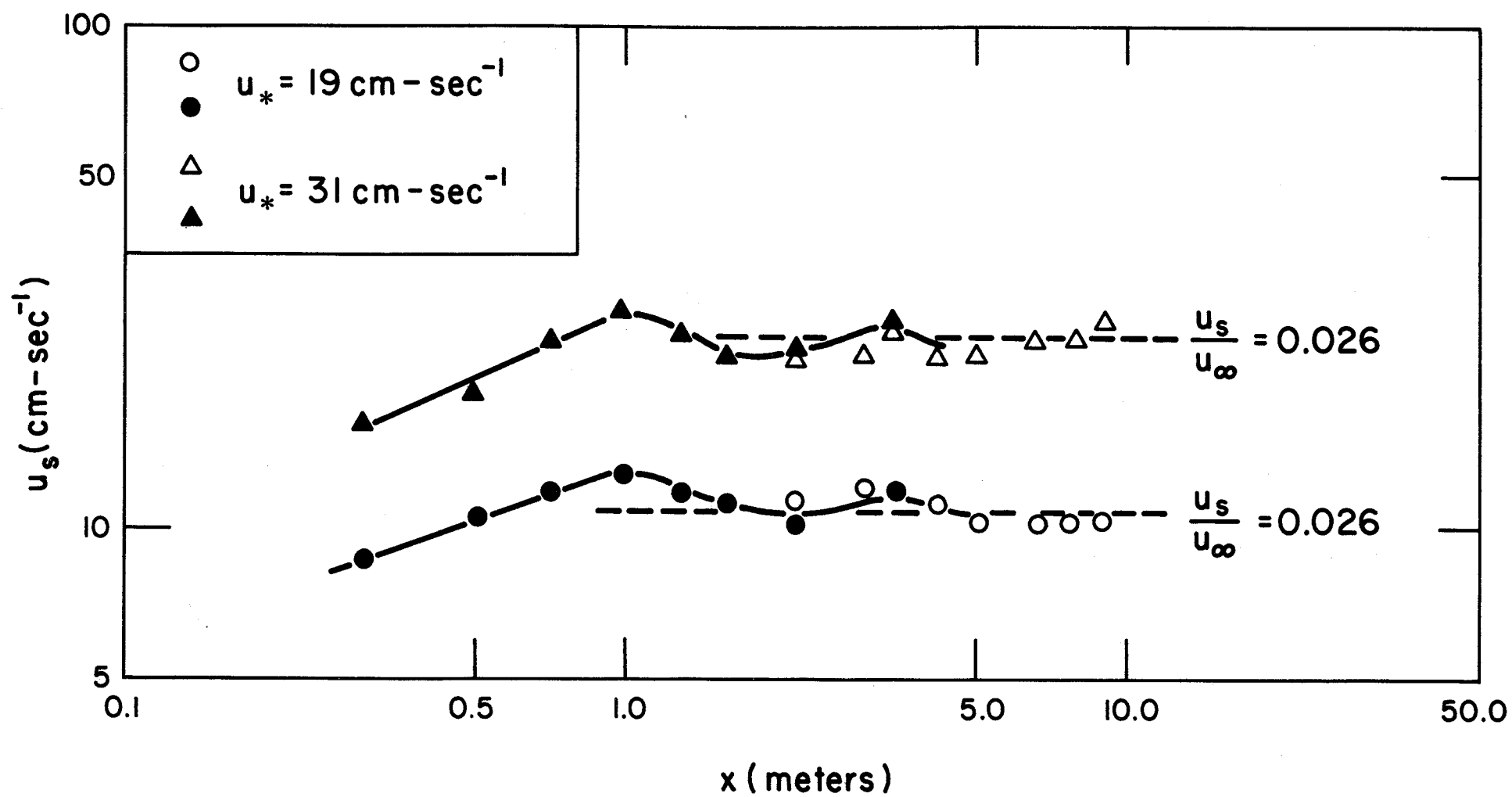


Figure 14

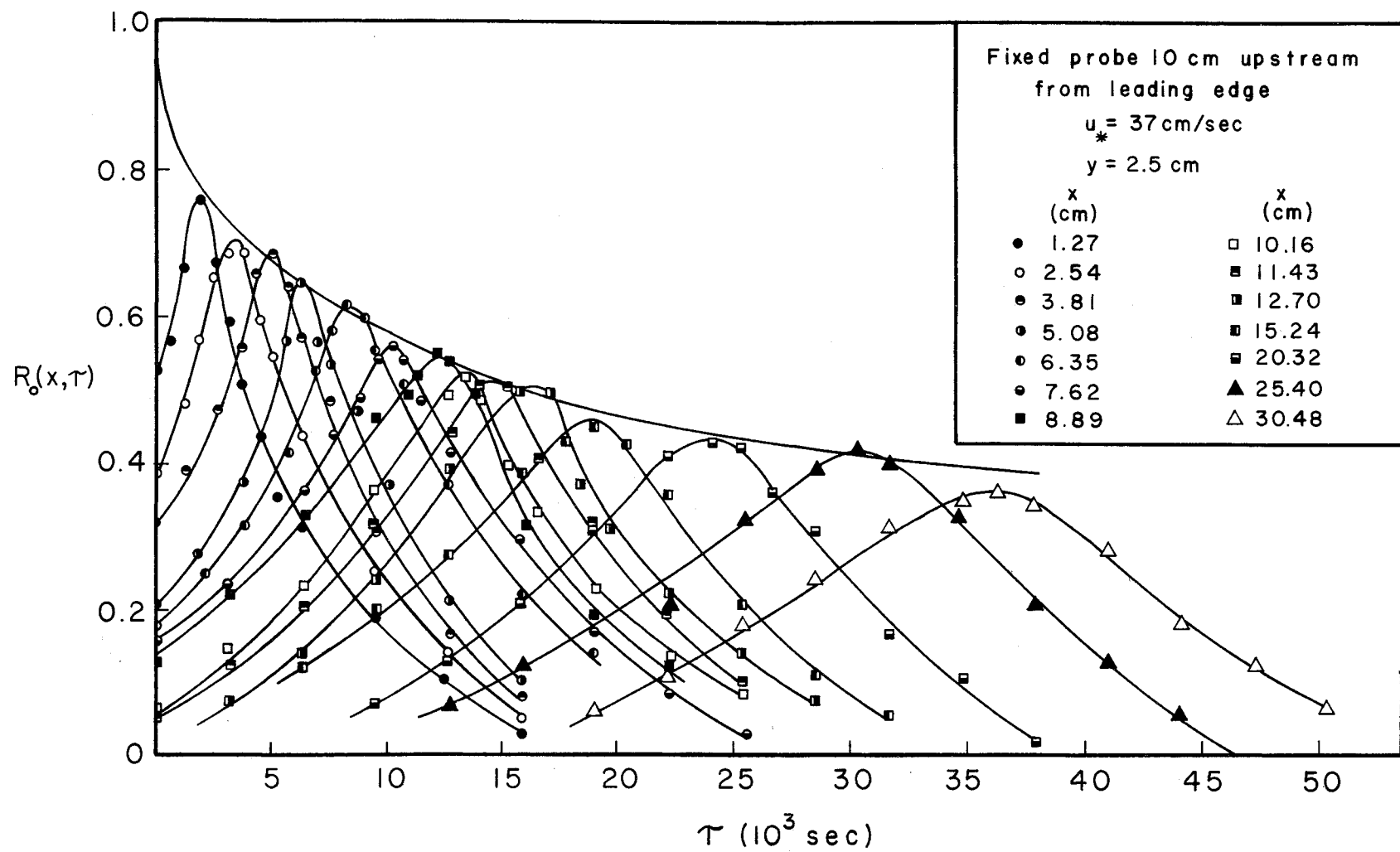


Figure 15

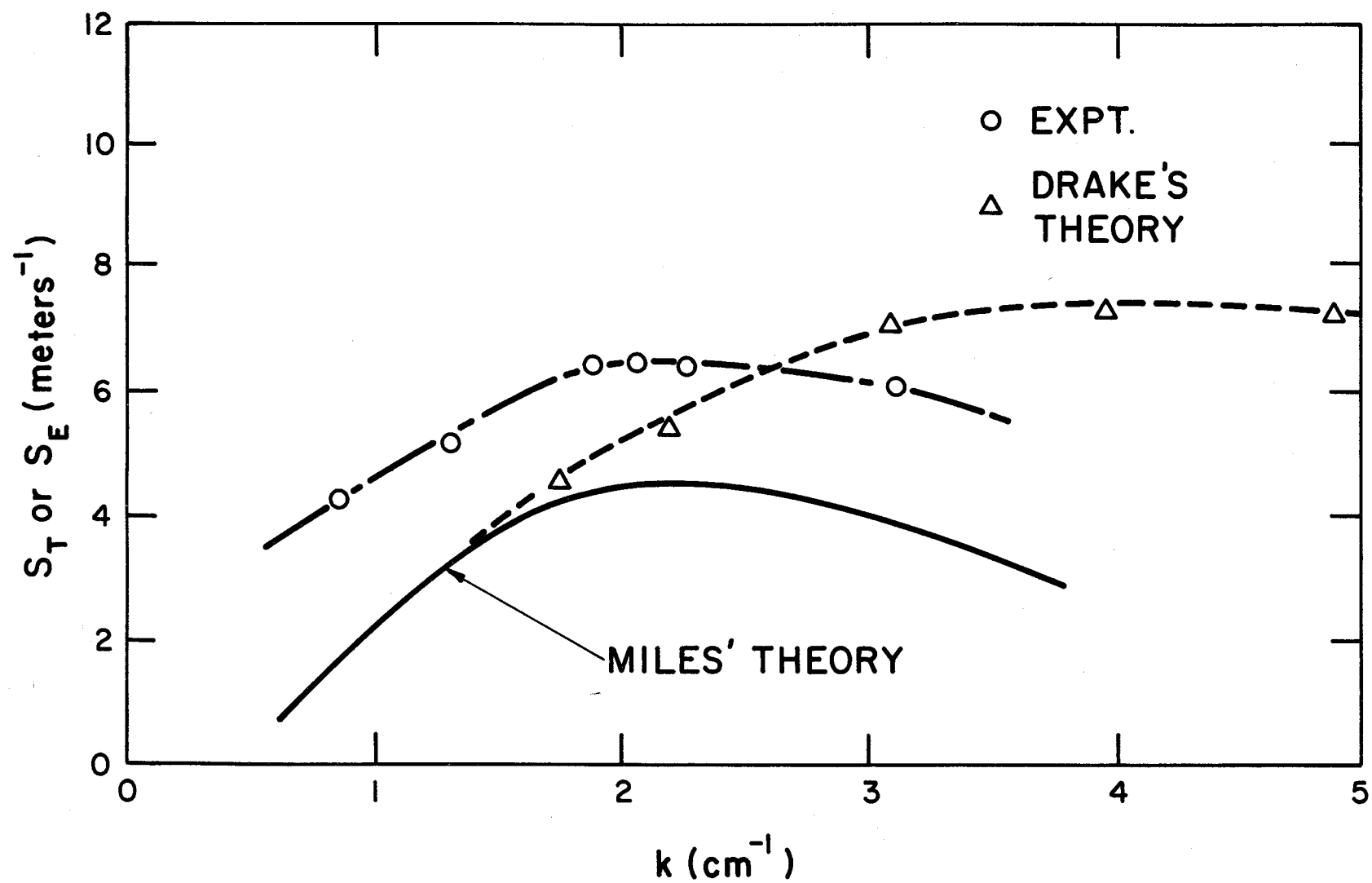


Figure 16